

AD-A255 668



2

PL-TR-92-2023

Super-Micro Computer Weather Prediction Model

Keith L. Seitter and Frank P. Colby, Jr.

University of Massachusetts - Lowell
Department of Earth Sciences
One University Avenue
Lowell, MA 01854

January 1992

DTIC
ELECTE
AUG 12 1992
S A D

Final Report

17 May 1988-30 November 1991

Approved for public release; distribution unlimited

92

8

10

102



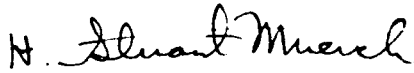
PHILLIPS LABORATORY
AIR FORCE SYSTEMS COMMAND
HANSCOM AIR FORCE BASE, MASSACHUSETTS 01731-5000

92-22626



~~435343~~

This technical report has been reviewed and is approved for publication.



H. STUART MUENCH
Contract Manager



DONALD A. CHISHOLM
Chief, Atmospheric Prediction Branch
Atmospheric Sciences Division



ROBERT A. McCLATCHEY
Director, Atmospheric Sciences Division

This document has been reviewed by the ESD Public Affairs Office (PA) and is releasable to the National Technical Information Service (NTIS).

Qualified requestors may obtain additional copies from the Defense Technical Information Center. All others should apply to the National Technical Information Service.

If your address has changed, or if you wish to be removed from the mailing list, or if the addressee is no longer employed by your organization, please notify PL/TSI, Hanscom AFB, MA 01731-5000. This will assist us in maintaining a current mailing list.

Do not return copies of this report unless contractual obligations or notices on a specific document requires that it be returned.

REPORT DOCUMENTATION PAGE			Form Approved OMB No. 0704-0188	
<small>The reporting burden for this collection of information is estimated to average 1 hour per response, including the time for reviewing instructions, searching existing data sources, gathering and maintaining the data needed, and completing and reviewing the collection of information. Send comments regarding this burden estimate or any other aspect of this collection of information, including suggestions for reducing this burden, to Washington Headquarters Services, Directorate for Information Operations and Reports, 1215 Jefferson Highway, Suite 1204, Arlington, VA 22202-4302, and to the Office of Management and Budget, Paperwork Project, (0704-0188), Washington, DC 20503.</small>				
1. AGENCY USE ONLY (Leave blank)	2. REPORT DATE January 1992	3. REPORT TYPE AND DATES COVERED Scientific Final (5/17/88 - 11/30/91)		
4. TITLE AND SUBTITLE Super-Micro Computer Weather Prediction Model		5. FUNDING NUMBERS PL 61101F PL 61101F-1A-1-0100AA Contract DMR-88-01001F		
6. AUTHOR(S) Keith L. Seitter Frank P. Colby, Jr.				
7. PERFORMING ORGANIZATION NAME(S) AND ADDRESS(ES) University of Massachusetts - Lowell Department of Earth Sciences One University Avenue Lowell, MA 01854		8. PERFORMING ORGANIZATION REPORT NUMBER		
9. SPONSORING/MONITORING AGENCY NAME(S) AND ADDRESS(ES) Phillips Laboratory Hanscom AFB, MA 01731-5000 Contract Manager: H. Stuart Muench/GPAP		10. SPONSORING/MONITORING AGENCY REPORT NUMBER PL-TR-92-2023		
11. SUPPLEMENTARY NOTES				
12a. DISTRIBUTION/AVAILABILITY STATEMENT Approved for public release, distribution unlimited		12b. DISTRIBUTION CODE		
13. ABSTRACT (Maximum 200 words) A meso-beta scale numerical model is described that is designed specifically for operational use on relatively small computers. A major aspect of the model is that it treats the boundary layer as a single model layer of known structure whose depth can evolve during the integration. The model equations are recast in a coordinate system, referred to as boundary-layer coordinates, based on the depth of the evolving boundary layer. The model described here does not include condensation processes, but it does include a radiation parameterization schemes governing the structure of the stable and unstable boundary layers and the transitions between these regimes, and parameterizations for the fluxes of heat and moisture between the boundary layer and the earth's surface. Simulations have been carried out with a prototype model that has five layers and 20 km resolution in the fine grid mesh of its nested domain. The results of these simulations show that the model is capable of reproducing such mesoscale phenomena as mountain lee waves and the Florida sea-breeze circulation fairly well. Results are also presented of some preliminary simulations for the complex terrain of southern New England that demonstrate the need for carefully prepared terrain fields in numerical models.				
14. SUBJECT TERMS numerical weather prediction computer simulation models boundary-layer parameterization		mesoscale modeling weather forecasting		15. NUMBER OF PAGES 80
				16. PRICE CODE
17. SECURITY CLASSIFICATION OF REPORT Unclassified	18. SECURITY CLASSIFICATION OF THIS PAGE Unclassified	19. SECURITY CLASSIFICATION OF ABSTRACT Unclassified	20. LIMITATION OF ABSTRACT SAR	

CONTENTS

1. Introduction	1
2. Model Description	4
a. Basic model equations	4
b. Grid domain and horizontal nesting	7
c. Time integration and outer lateral boundary conditions	9
d. Coupling of the model with the boundary-layer parameterizations	10
e. Horizontal diffusion	12
3. Boundary-layer parameterization	12
a. Radiation	12
b. Surface energy balance	15
c. Frictional drag	18
d. Ground variables	18
e. Boundary-layer height	21
f. Boundary-layer variables	23
g. Boundary-layer transitions	23
4. Simulations with the model	25
a. Mountain lee-wave simulations	25
b. Sea-breeze simulations	29
5. Initial tests using realistic complex terrain	37
a. Test domain	37
b. Initial simulations and modifications to CGM terrain	46
6. Conclusions and future work	52
APPENDIX A: List of Variables	53
APPENDIX B: Derivation and Energy Conservation of the Eta-Coordinate System	57
a. Derivation of the equations in η -coordinates	57
b. Energy conservation in the η -system	59
c. The energy-conserving finite difference equations	61
d. The complete finite difference equation set	68
APPENDIX C: Creation of Terrain Fields	71
a. Creation of unmodified and envelope terrain	71
b. Smoothing and modification to ensure CGM/FGM compatibility	71
References	73

Accession For	
NTIS CP421	
DTIC TAB	
Unannounced	
Justification	
By	
Distribution/	
Availability Codes	
Dist	Avail and/or Special
A-1	

1. Introduction

Trajectory and advection models (Muench 1983; Muench and Chisholm 1985; Muench 1989) and automated display systems such as McIDAS and PROFS (Schlatter et al. 1985) show promise of providing added guidance for the very short term forecasting range of 0 to 6 hours. Full synoptic models such as the LFM and NGM have skill from about 12 hours to beyond 48 hours. However, both of these approaches fall short in the 6 to 18 hour period that is perhaps the most vital to the terminal forecaster. It is in this period that meso- β scale disturbances (such as fronts or squall lines) that are in the local area will have an immediate impact on the terminal forecast. Advection models begin failing after a few hours because of synoptic and mesoscale changes in wind patterns and because topographic and geographic influences are often not incorporated (Muench 1983; Muench 1989). On the other hand, the initialization of synoptic scale models is based on synoptic scale data that does not normally include mesoscale features present at the time of initialization, and the coarse grid spacing does not allow mesoscale features to develop during the integration. Hence, the synoptic scale model cannot be expected to forecast these mesoscale features. Other studies, however, have shown that mesoscale models can forecast the mesoscale structure of a variety of atmospheric phenomena even when initialized with observational data of only somewhat finer resolution than routinely used in synoptic scale models (Zhang and Fritsch 1986; and others).

There are currently many mesoscale numerical models within the research community [see Keyser and Uccellini (1987) for a discussion of some of these models]. Each of these models was developed initially to look at certain subsets of meteorological phenomena and then evolved into much more complex modeling systems capable of simulating a wide range of atmospheric conditions. While these models differ substantially in details, such as the level of complexity for the microphysical parameterizations or turbulence closure, they share some basic features. Most are what can be considered "research models" in that they are not

designed specifically for operational use; their primary use is to try to evaluate the role of various atmospheric processes for better understanding of the dynamics and physics of the atmosphere on the mesoscale. In general, these models tend to include the most realistic boundary layer, radiation, and microphysical parameterizations possible and still achieve acceptable computation times on the current generation of supercomputers. They are usually composed of at least one level of horizontal nesting and employ enough vertical layers to resolve explicitly the evolving boundary layer. Recently, the ETA mesoscale model (Mesinger et al. 1988; Mesinger et al. 1990) has been used in an operational mode (Kalnay et al. 1991), and a simplified version of the PSU/NCAR model has been used in a pseudo-operational setting (Warner and Seaman 1990). These models are somewhat simpler than the current generation of research models, but the ETA model still requires a supercomputer, and the simplified PSU/NCAR model requires significant computational time on a conventional mainframe.

The model described here represents a significant deviation from this approach. Here we attempt to develop a model specifically for operational use on the current or near-future generation of super-micro computers by making use of a consistent set of approximations and parameterizations that incorporates the physical understanding of mesoscale processes emerging from the results of research models. Our goal is a mesoscale model that is much faster computationally than research models but still has enough skill to provide guidance to the terminal forecaster in the 6–18 h forecast window. We seek to develop a mesoscale model that can be run locally by each forecast office, centered on its location, to provide local guidance.

Given the rapid increase in speed and power of small computers, it could be argued that the current research models could be run locally on relatively inexpensive computers within the next decade. There is currently some debate within the meteorological community on the relative merits of running highly complex mesoscale models locally at each forecast office compared to a centralized guidance with distributed products similar to those provided for synoptic scale models (McPherson 1991). Many argue that a very complex mesoscale model requiring a major data assimilation effort and excellent boundary conditions produced by synoptic scale models can only be maintained effectively at a national center. Further, these individuals argue that running a near-research-grade model

at many sites with largely overlapping domains is a waste of computer resources. This work supports this philosophy of mesoscale guidance, but argues that simplified, computationally fast, mesoscale models can provide a valued-added service when run at local forecast offices. While the simple model described in this report cannot be expected to give as skillful guidance over a forecast period as a research grade model, it can be run locally long before the more complex model output is available, providing a "first look"—similar to the way the National Meteorological Center's LFM model is used operationally today (Petersen and Stackpole 1989). With future advances, a model of the type developed here could possibly be run in an interactive fashion—similar to interactive sounding modification programs now available that allow the forecaster to investigate "what if" scenarios.

While it is possible to produce a simplified version of a research model that is computationally efficient enough to provide operational mesoscale forecasts (Warner and Seaman 1990), we have taken a different approach. Several studies have identified topographic forcing and boundary-layer processes as major contributors to mesoscale structure (Gauntlet et al. 1984; Ookouchi et al. 1984; Benjamin and Carlson 1986; Nickerson et al. 1986; and others), so any successful mesoscale model must include these processes. The sigma-coordinate system used in many models allows topography to be included in a straightforward manner. Most models use many layers near the surface to resolve boundary-layer processes, but this adds to the computational expense by increasing the number of grid points in the model. Our approach is to treat the boundary layer as a single layer of known structure that can evolve over the course of the integration. The model equations are recast in a coordinate system based on the depth of the evolving boundary layer. This allows the boundary-layer structure and fluxes to be represented in a way similar to that used in some mixed-layer models (Lavoie 1972; Colby 1984; and others) so that the physical processes are represented without the computational expense associated with a large number of vertical layers.

This paper describes a prototype dry mesoscale model that has been developed using this approach. Section 2 introduces the boundary-layer coordinate system on which the model is based and presents the numerical details of the model. Section 3 summarizes the boundary layer and radiation parameterizations employed in the model. This is followed, in section 4, by the results of simulations designed

to assess the capabilities of the model. Section 5, gives the results of some very preliminary tests using complex terrain and describes how the terrain field must be adjusted to be consistent with the boundary conditions. The paper concludes with discussion and plans for extensions to the dry model.

2. Model description

a. Basic model equations

As discussed in the Introduction, most mesoscale models rely on a large number of layers near the surface in order to resolve explicitly the growth and decay of the planetary boundary layer and to simulate correctly the fluxes of heat and moisture that couple the atmosphere to the surface. This leads to models with a large number of layers in the vertical, resulting in large numbers of computations per timestep and relatively long computation times even in supercomputer environments (Peilke 1984; his Appendix B). On the other hand, some early models showed success in simulating nonboundary-layer-driven flows (such as mountain lee-waves) with relatively few layers (Anthes and Warner 1978), and other models looking specifically at boundary-layer processes were able to capture successfully the important features by treating the boundary layer as a single layer which could dynamically grow and collapse (Lavoie 1972; Keyser and Anthes 1977; Anthes et al. 1982; Colby 1984).

The present formulation seeks to marry these two approaches into a single three-dimensional mesoscale model. The lowest layer of the model is the boundary layer—it is allowed to grow in depth or collapse at each grid point as the simulation proceeds in response to changes produced by the boundary-layer and radiation parameterizations. The layers above the boundary layer adjust dynamically to the changing boundary-layer depth, while simulating the horizontal and vertical advections of momentum and thermodynamic variables and maintaining the proper balances that hold at the meso- β scale.

The vertical coordinate that allows for this changing boundary-layer depth is a modification of the common σ -coordinate [$\sigma = (p - p_t) / (p_s - p_t)$ where p_s is the surface pressure and p_t is a pressure level specified as the top of the model (we

take $p_t = 100$ mb for this study)). If we let σ_h represent the height of the top of the boundary layer in σ (see Fig.1), we can define a new vertical coordinate, η , as

$$\eta = \frac{\sigma - \sigma_h}{H} \quad H = \begin{cases} \sigma_h & \sigma < \sigma_h \\ 1 - \sigma_h & \sigma > \sigma_h \end{cases} \quad (2.1)$$

We refer to the η coordinate system as "boundary-layer coordinates" [note that this is not related to what have been called ETA models (Mesinger et al. 1988; Mesinger et al. 1990)] The vector momentum equation, hydrostatic relation, continuity equation, thermodynamic equation, and specific humidity conservation equation can be written in the η system as (see appendix B for details on the derivation of this set)

$$\begin{aligned} \frac{\partial \pi H V}{\partial t} + \frac{\partial u \pi H V}{\partial x} + \frac{\partial v \pi H V}{\partial y} + \frac{\partial \pi V H \dot{\eta}}{\partial \eta} = \\ - \pi H \nabla \phi - \pi H \alpha \nabla \sigma \pi - f \mathbf{k} \times \pi H V + \pi H F_{uv} \end{aligned} \quad (2.2)$$

$$\frac{\partial \phi}{\partial \eta} = -\pi H \alpha \quad (2.3)$$

$$\frac{\partial \pi H}{\partial t} + \nabla \cdot \pi H V + \pi \frac{\partial H \dot{\eta}}{\partial \eta} = 0 \quad (2.4)$$

$$\frac{\partial \pi H T}{\partial t} + \frac{\partial u \pi H T}{\partial x} + \frac{\partial v \pi H T}{\partial y} + \frac{\partial \pi T H \dot{\eta}}{\partial \eta} = \frac{\pi H \alpha}{c_p} \omega + \frac{\pi H Q}{c_p} + \pi H F_T \quad (2.5)$$

$$\frac{\partial \pi H q}{\partial t} + \frac{\partial u \pi H q}{\partial x} + \frac{\partial v \pi H q}{\partial y} + \frac{\partial \pi q H \dot{\eta}}{\partial \eta} = 0 \quad (2.6)$$

where $\pi = p_s - p_t$, and the other terms have their normal meteorological definitions (see Appendix A for a list of variables). It should be noted that the σ which appears on the right-hand side of (2.2) is a dependent variable which, in general, will not be constant on a constant- η surface. Expansion of this gradient of a product results in an additional pressure-gradient-force type term not present in traditional σ -coordinate models. It should also be noted that the humidity is treated here as a passive scalar, so (2.6) simply represents conservation of q (that is, $dq/dt = 0$) in the η system. When condensation and evaporation are included, appropriate source and sink terms need to be added to the rhs of (2.6) and another conservation equation governing the condensate is required.

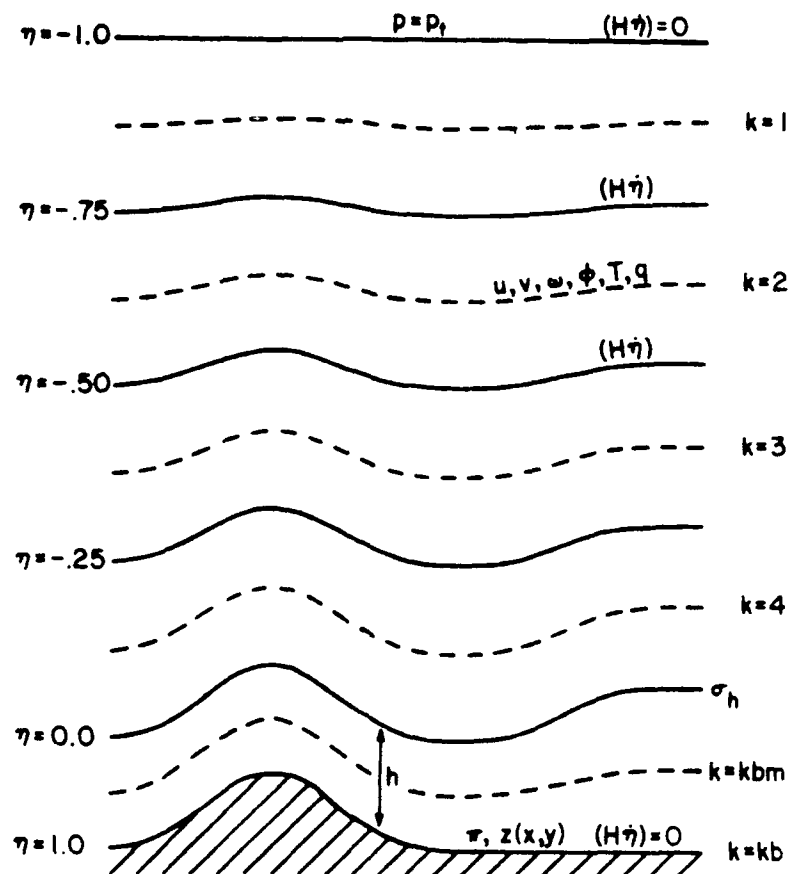


Fig. 1. Schematic structure of the five-layer η -coordinate model.

Equation (2.4) is not used directly in the model, but it does provide the means of calculating vertical velocities and the rate of change of surface pressure. Integration of (2.4) from the model top to the surface yields

$$\begin{aligned} \frac{\partial \pi}{\partial t} = & - \int_{-1}^0 \left[\frac{\partial}{\partial x} (H_1 \pi u) + \frac{\partial}{\partial y} (H_1 \pi v) \right] d\eta \\ & - \int_0^1 \left[\frac{\partial}{\partial x} (H_2 \pi u) + \frac{\partial}{\partial y} (H_2 \pi v) \right] d\eta \end{aligned} \quad (2.7)$$

where $H_1 = (1 - \sigma_h)$ and $H_2 = \sigma_h$ represent the values of H above and below the boundary-layer top, respectively, as given by (2.1). Integration of (2.4) from the top of the model down to a specific interface level, along with the use of $\partial \pi / \partial t$ found with (2.7) allows the determination of $(H\dot{\eta})$ at each interface as

$$(H\dot{\eta}) = -(\eta+1) \left[\pi \frac{\partial \sigma_h}{\partial t} + \frac{H_1 \partial \pi}{\pi \partial t} \right] - \int_{-1}^{\eta} \left[\frac{\partial}{\partial x} (H_1 \pi u) + \frac{\partial}{\partial y} (H_1 \pi v) \right] d\eta \quad (2.8)$$

It is not difficult to show that the continuous equations in boundary-layer coordinates satisfy the proper energy conservation constraints (Colby and Seitter, 1990). It is desirable to have the finite difference forms of the equations satisfy these energy conservation constraints as well, which can provide guidance on the form the finite difference equations should take. In particular, the energy constraints lead to specific forms for the solution of the thermodynamic equation, (2.5), and the integration of the hydrostatic equation, (2.3), to find the geopotentials of midlevels of the η -layers. The resulting finite difference forms are considerably different in structure from equations (2.2)–(2.6), and are given in Appendix B.

The last terms on the rhs of (2.2), and (2.5) include a "friction" term, F , which, above the boundary layer, is given by a horizontal eddy diffusion. This term is modeled by a simple Fickian diffusion, $K \nabla^2 \phi$, where K is a constant eddy viscosity and ϕ is the variable of interest (u , v , or T).

b. Grid domain and horizontal nesting

A staggered grid is used in both the vertical and horizontal directions. In the vertical, all variables are layer quantities except vertical velocities, which are defined at interface levels (see Fig. 1). Although the coordinate system is quite general and would allow multiple layers in the boundary layer ($1 > \eta > 0$), we currently run the model with the boundary layer representing a single model layer and specify four layers above the boundary layer that are equally spaced in η . Horizontally, velocities are defined on staggered points that surround the points on which all other variables are defined, as in Anthes and Warner (1978). In order to increase the overall model domain size and move the lateral boundaries away from the area of primary interest, a horizontal nesting of the model is employed as developed by Zhang et al. (1986). A fine grid mesh (FGM) with 20 km resolution is nested in a coarse grid mesh (CGM) with 60 km resolution. The complete nested staggered grid domain, showing all points, is shown in Fig. 2. A 3:1 ratio of FGM points to CGM points is necessary with a staggered grid so that both "velocity" (x's in Fig. 2) and "thermodynamic" (o's in Fig. 2) points can be coincident in the overlap region (Zhang et al. 1986). The CGM domain covers 1320 km x 1320 km while the

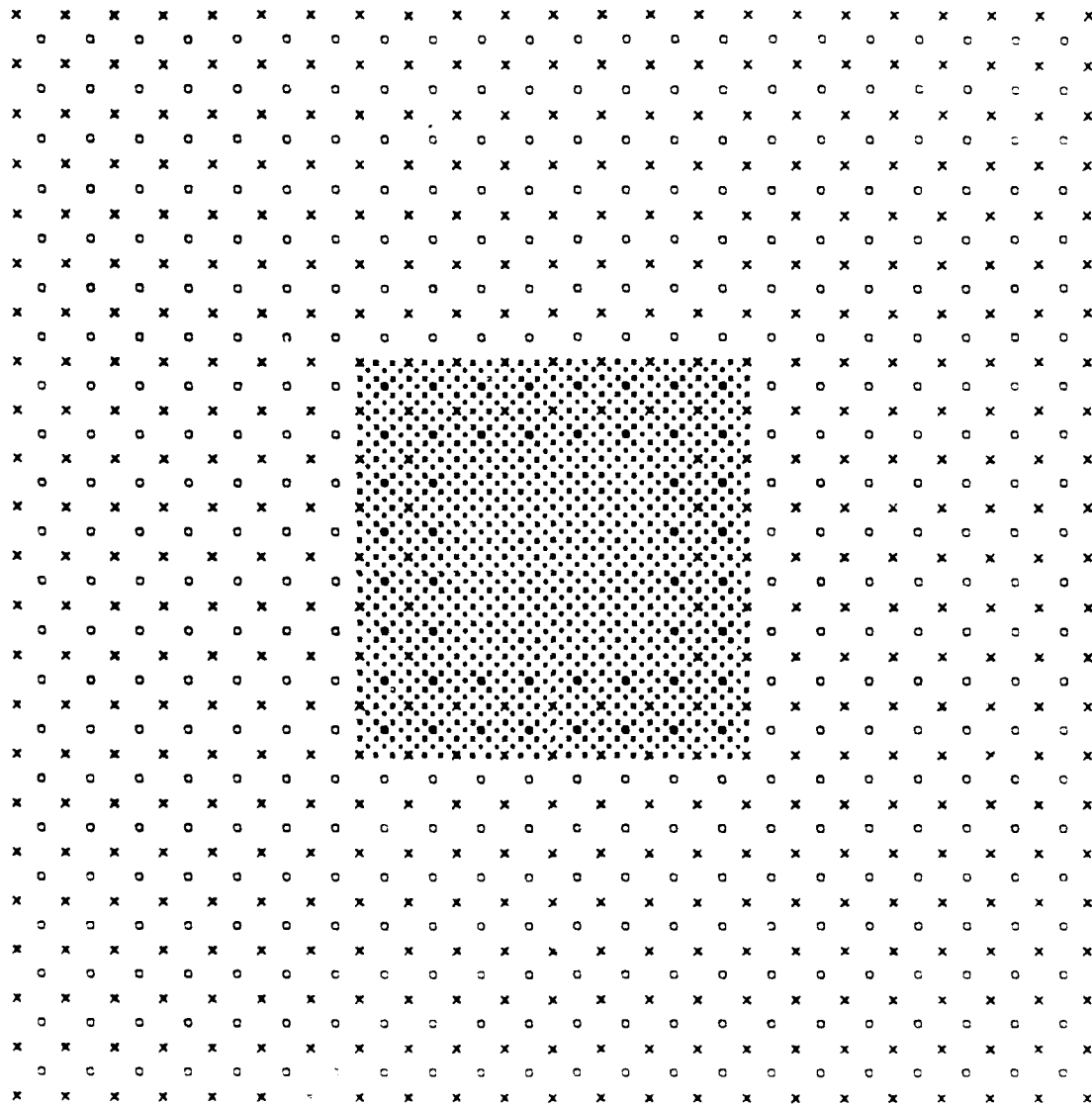


Fig. 2. Horizontal plot of the nested staggered grid structure used in the model. Velocities are specified on all "x" points and all other variables are defined on "o" points (referred to as "thermodynamic" points in the text).

FGM domain is 480 km x 480 km for "thermodynamic" points (all displays will be made on "thermodynamic" point arrays, with any displayed velocities being averaged to these points).

The two-way interactive nesting procedure of Zhang et al. (1986) is used with a few minor modifications. In the calculation of tendencies for the "thermodynamic" points in the FGM, for example, a simple linear interpolation is used between CGM points nearest the boundary FGM point rather than the "Lagrangian interpolation" used by Zhang et al. (1986). Also, rather than use a Newtonian damping scheme near the boundaries, the eddy diffusion coefficient K is increased for FGM points within two grid intervals of the FGM/CGM interface. This increased diffusion is applied only in the momentum equation to help control noise resulting from the overspecification there, and has a net effect quite similar to the Newtonian damping term used by Zhang et al. (see Colby and Seitter 1990; Kurihara and Bender 1980).

c. Time integration and outer lateral boundary condition

Time integration for the model is performed using the leapfrog scheme with an Asselin filter except for the moisture equation (2.6), which employs a forward timestepping scheme with upstream differencing. The Asselin filter factor is set to 0.5 as suggested by Schlesinger et al. (1983) for models employing moderate diffusion. The time step for FGM points is 20 s and for CGM points is 60 s. The flow relaxation condition of Davies (1976) is used on the lateral boundaries of the CGM following the work of Seitter (1987) who found that this condition was well-behaved, provided a simple means of allowing external information to be introduced into the model, and did not require the smoothing operator necessary in the Perkey and Kreitzberg (1976) sponge. The flow relaxation condition is normally applied over a 5 gridpoint wide region near the boundary, and solutions in this "relaxation region" should be considered modified. The flow relaxation condition is only applied at the lateral boundaries of the CGM domain, however, so FGM points are not significantly influenced by the relaxation region.

Experimentation has shown that application of the condition over a 6 gridpoint wide region yields a slightly improved transition between the interior and boundary areas, even though the weight on the sixth gridpoint from the boundary is very small. The weights on the staggered gridpoints are set so that they smoothly

match the logarithmic decrease of the weighting function from the boundary to the interior.

d. Coupling of the model with the boundary-layer parameterization

The basic equations that make up the boundary-layer parameterization are described in detail in section 3. The boundary-layer package provides the model with the fluxes of heat, moisture, and momentum from the surface, and calculates the rate of change of boundary-layer height, which is fundamental to the boundary-layer coordinate formulation. It also provides tendencies for the ground surface temperature and ground wetness, which are then timestepped using a leapfrog scheme with Asselin filter just as the other prognostic variables in the model. A summary of these quantities is shown in Table 1.

It is important to note that the boundary-layer routine diagnoses the current boundary-layer depth (hydrostatically) from the current σ_h , and returns a time rate of change of boundary-layer height, $\partial h / \partial t$, where h is in geometric height above the ground. The model requires both the rate of change of boundary-layer height and the new boundary-layer height in terms of σ , so a conversion must be made.

The hydrostatic relation may be written in σ -coordinates as

$$\frac{\partial \phi}{\partial \sigma} = -\pi \alpha \quad (2.9)$$

which can be integrated from the surface ($\sigma=1$) to the top of the boundary layer ($\sigma=\sigma_h$) to obtain

$$\phi_h - \phi_s = -\pi \int_1^{\sigma_h} \alpha d\sigma \quad (2.10)$$

where ϕ_s is the geopotential of the surface and ϕ_h is the geopotential of the boundary-layer top. With the excellent approximation that $(\phi_h - \phi_s) = gh$, and making use of the mean value theorem, we can obtain

$$h = \frac{\pi \bar{\alpha}}{g} (1 - \sigma_h) \quad (2.11)$$

Taking the partial derivative with respect to time of this expression and

Table 1. Quantities provided to the model by the boundary-layer parameterization.

Variable returned	Description
$\frac{dh}{dt}$	Rate of change in height of boundary layer top
$\frac{dT_G}{dt}$	Rate of change of ground temperature
$\frac{dGW}{dt}$	Rate of change of ground wetness
T_{kb}	Diagnosed "surface" temperature
q_{kb}	Diagnosed "surface" mixing ratio
SH	Sensible heat flux
LH	Latent heat flux
GS	Surface soil heat flux
NR	Net radiation (incoming shortwave minus outgoing IR)
τ_{xy}	Surface stress (friction)

rearranging yields

$$\frac{\partial \sigma_h}{\partial t} = -\frac{g}{\pi \bar{\alpha}} \frac{\partial h}{\partial t} + \frac{(1 - \sigma_h) \partial \pi}{\pi \partial t} + \frac{(1 - \sigma_h) \partial \bar{\alpha}}{\bar{\alpha} \partial t} \quad (2.12)$$

Equation (2.12) provides a means of computing the rate of change of σ_h from $\partial h / \partial t$ provided we can estimate all the other terms on the rhs. Experimentation has shown that the last term is always at least two orders of magnitude smaller than the first two terms on the rhs, so that term is dropped. The remaining information is readily available from the model since the boundary-layer temperature can be used to find $\bar{\alpha}$ and $\partial \pi / \partial t$ can be computed using (2.7). The tendency produced by (2.12) is used on the current timestep where required [for example in (2.8)], and it is also used to calculate the new value of σ_h in a leapfrog timestepping scheme (with Asselin filter) identical to that used for the other prognostic variables. A horizontal diffusion of the form $K \nabla^2 \sigma_h$ is applied to the tendency of σ_h , with $K = 2 \times 10^5 \text{ m}^2 \text{ s}^{-1}$. This weakly couples the boundary-layer height to the surrounding

grid points and suppresses exceedingly sharp gradients or noise in the boundary-layer height field.

e. Horizontal diffusion

After experimentation with simulations of a variety of atmospheric phenomena (Colby and Seitter 1990), the eddy diffusion coefficient was set at $K = 2 \times 10^5 \text{ m}^2 \text{ s}^{-1}$ for the momentum components in the FGM. This yields a nondimensional eddy viscosity of 0.01 which is somewhat smaller than the value used by Anthes and Warner (1978) in their six-layer model. The eddy diffusion coefficient in the CGM is set to $K = 6 \times 10^5 \text{ m}^2 \text{ s}^{-1}$ for the momentum components in order to yield the same nondimensional eddy viscosity there. The diffusion of temperature uses an eddy diffusion coefficient one order of magnitude smaller than that used for the momentum components.

3. Boundary-layer parameterization

The boundary-layer parameterization is composed of several parts: radiation; surface energy and moisture balance; surface drag; surface temperature and specific humidity; and boundary-layer height change. Each of the formulations, described in the following subsections, is designed to balance computational speed with physical accuracy. In most cases, the physical accuracy is restricted by the limited vertical resolution of the model rather than by the mathematical formulation. The boundary-layer parameterization package has been tested in a one-dimensional form against data taken during the O'Neill boundary layer experiment (Lettau and Davidson 1957) and found to reproduce the evolution of the boundary-layer structure and surface temperature and moisture quite well (Colby and Seitter 1990).

a. Radiation

The radiation parameterization is taken from Katayama (1972) and is a routine originally designed for use in the UCLA general circulation model. Although the results presented in this paper are for a prototype model with no condensation processes, the radiation parameterization allows for cloud layers, and the following

discussion describes this more complete form. The incident radiation and infra-red (IR) emission are calculated separately. The model incorporates an exponential fit to the data for specific humidity to allow simple integration of water content. The concentration of CO_2 is included in a fixed form based on experimental data, and its contribution is then a constant.

The influx of radiation is computed by starting with the solar constant and modifying it for albedo at the top of the atmosphere. Scattered and absorbable radiation are computed separately, the fraction being assumed constant (35% available for absorption, 65% scattered to the ground). The scattered part of the incident radiation is corrected for multiple reflection between the atmosphere and the ground and given by

$$\text{GLW}_s = (0.651)S_0\cos(ZT)\left(\frac{1-\alpha_s}{1-\alpha_s\alpha_g}\right) \quad (3.1)$$

If a cloud layer is present (in future moist versions of the model), its presence is felt by both scattered and absorbable components. If the cloud is thick enough, and covers enough sky, incident radiation can be reduced to zero. The model allows for variable amounts of cloud in each atmospheric layer expressed as a percentage. Low and middle level clouds can be included as a single layer covering all or part of the sky. The cloud layer directly affects both scattered and absorbable shortwave radiation.

Fractional absorption by water vapor is calculated by

$$\text{ABS}(k) = (0.271)\left[\frac{E_{H_2O}(k)}{\cos(ZT)}\right]^{0.303} \quad (3.2)$$

where E_{H_2O} is the effective amount of water vapor in layer k . The radiation that is finally absorbed in the soil becomes one component of the surface energy balance. The absorbed part of the incident radiation at the ground is

$$\text{GLW}_a = (0.349)S_0\cos(ZT) - \sum_k \text{ABS}(k) \quad (3.3)$$

where the sum is taken over all layers. The total absorption at the ground is then

$$\text{GAB} = (1-\alpha_g)(\text{GLW}_s + \text{GLW}_a) \quad (3.4)$$

To find the IR flux, the equation of radiative transfer is solved subject to the boundary conditions that downward IR flux at the top of the atmosphere is zero, and the upward IR flux at the earth's surface is the black-body radiation at the surface temperature. Weighted transmission functions are used, corrected for the pressure dependence of absorption. The total transmission function is assumed to be the product of the individual ones for CO₂ and H₂O. Downward flux is

$$IR_d = \pi B_z - \pi B_o \bar{\tau}(u_\infty^* - u_z^*, T_o) - (\pi B_\infty - \pi B_o) \tau(u_\infty^* - u_z^*, \bar{T}) \\ + \int \frac{\pi B_\infty}{\pi B_z} \tau(u^* - u_z^*, \bar{T}) d(\pi B) \quad (3.5)$$

where for each layer, $\pi B_i = \sigma T_i^4$. The weak region is 210–320 K for water vapor, so letting $T_c = 220$ K, the weak dependence region need only have a mean temperature specified (\bar{T}). Similarly, the upward flux is

$$IR_u = \pi B_z + \int \frac{\pi B_o}{\pi B_z} \tau(u^* - u_z^*, \bar{T}) d(\pi B) \quad (3.6)$$

and the net upward flux is

$$IR_z = IR_u - IR_d \quad (3.7)$$

The only difficulty is determining the proper transmission function near the particular level where τ varies exponentially. The model uses an interpolation factor that is an empirical function of pressure, mixing ratio and layer thickness. This allows proper calculation of τ without a fine vertical mesh. The mean transmission functions are defined by empirical formulae at $T_c = 220$ K and $\bar{T} = 260$ K. Temperature dependence of τ for CO₂ is neglected, so a mean τ for CO₂ is used based on pressure and amount of CO₂. The distribution of CO₂ at each level is a constant.

The IR flux is computed only for the surface, since the IR cooling rates in the free atmosphere are insignificant on diurnal time scales. This saves considerable computation time. The net radiation is then

$$NR = GAB - IR_g \quad (3.8)$$

Radiation calculations were made with the above scheme for a varying number of atmospheric layers. These calculations showed that when layers were thicker than 100 mb, more significant errors occurred in the net radiation values. Comparisons were made, for example, using a sounding that originally had 19 unevenly spaced levels. Reducing this to only 7 levels produced NR values in error by nearly 15% compared to the 19-level result. This error is probably acceptable for most situations since it implies a fairly small error in the surface temperature change due to radiation and because the model will not be integrated for more than about 24 h. This error can be improved somewhat, however, without the need for more detail in the sounding. If the routine started with the same 7 levels, but was allowed to linearly interpolate a new level in the middle of any layer thicker than 100 mb, the error in NR was reduced to less than 10%—despite the fact that no additional vertical resolution in temperature was available.

b. Surface energy balance

The surface energy balance has the form

$$NR = SH + LH + GS \quad (3.9)$$

where SH is the sensible heat flux upward from the surface, LH is the latent heat flux upward from the surface, and GS is the soil heat flux downward into the ground (heating the soil). The quantity NR is determined from the radiation parameterization [see Eq. (3.8)].

The sensible heat flux and latent heat flux (SH, LH) are parameterized using Monin-Obukhov similarity theory for the planetary boundary layer (PBL). The fluxes depend on the vertical gradients of temperature and specific humidity in the surface layer, the wind in the model layer directly above the PBL, and the stability of the boundary layer. The theory assumes that the structure of temperature and moisture in the PBL have forms that can be described by universal structure functions when scaled equations are used. There are actually two structures involved, since the PBL contains at least two distinct layers—the surface layer and the boundary layer (see Fig. 3). Although the parameterization does not include an explicit surface layer, one is assumed to be present. This “surface layer” is assumed to be a constant 5 mb thick. If the functions are required to be matched

at their common boundary, the following results are obtained

$$\frac{u_{g0}}{u_*} = \frac{1}{k} \left[\ln \left| \frac{u_*}{f z_0} \right| - A(\mu) \right] \quad (3.10)$$

$$\frac{v_{g0}}{u_*} = - \frac{B(\mu)}{k} \text{Sign} f \quad (3.11)$$

$$\frac{\theta_\infty - \theta_0}{\theta_*} = \frac{1}{k} C \left[\ln \left| \frac{u_*}{f z_0} \right| - C(\mu) \right] \quad (3.12)$$

$$\frac{u_{g0}}{u_*} = \frac{1}{k} \left[\ln \frac{h}{z_0} - A_i(\mu_i) \right] \quad (3.13)$$

$$\frac{v_{g0}}{u_*} = - \frac{B_i(\mu_i)}{k} \text{Sign} f \quad (3.14)$$

$$\frac{\theta_\infty - \theta_0}{\theta_*} = \frac{1}{k} C \left[\ln \frac{h}{z_0} - C_i(\mu_i) \right] \quad (3.15)$$

where

u_{g0}, v_{g0} = components of the surface geostrophic wind

$A(\mu), B(\mu), C(\mu)$ = universal functions for a stable boundary layer

$A_i(\mu_i), B_i(\mu_i), C_i(\mu_i)$ = universal functions for an unstable boundary layer

where the universal functions are those given by Arya (1975).

To determine the fluxes, we use inverted forms of these equations that are based on two parameters:

$$\text{stable case} \quad S = \frac{g(\theta_\infty - \theta_0)}{\theta |f| V_a} \quad (3.16)$$

$$\text{unstable case} \quad S_i = \frac{g(\theta_\infty - \theta_0)h}{V_a^2} \quad (3.17)$$

and

$$\text{stable and unstable} \quad R_o = \frac{V_a}{|f| z_0} \quad (3.18)$$

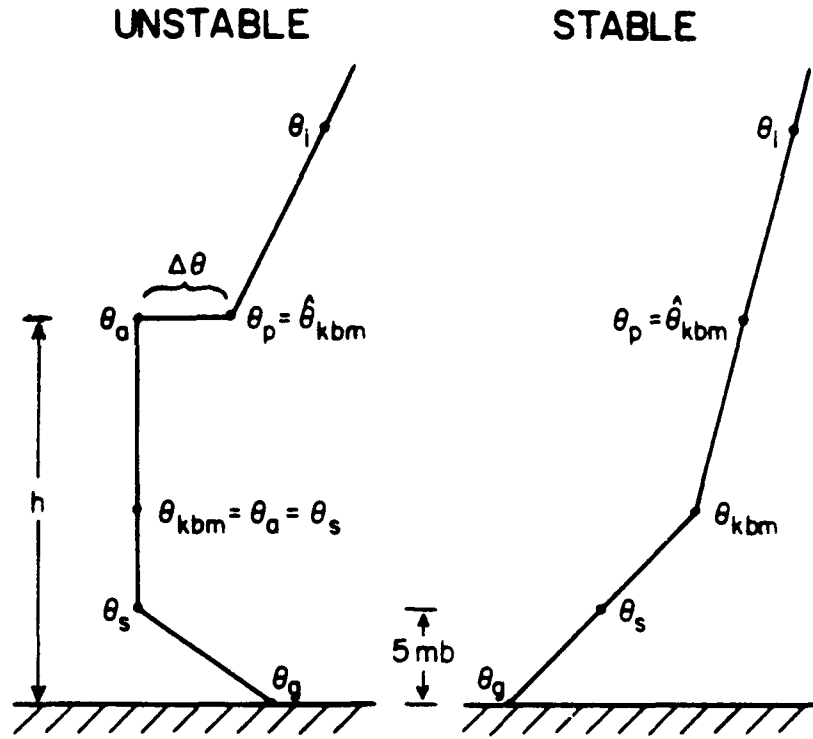


Fig. 3. Schematic of boundary layer structure for (a) stable and (b) unstable cases.

The inverted equations have the form

$$\frac{|\vec{\tau}_{xy}|}{\rho V_\alpha^2} = C_f(R_o, S) \quad (3.19)$$

$$\tan^{-1} \left(\frac{v_{g0}}{u_{g0}} \right) = \alpha_0(R_o, S) \quad (3.20)$$

$$- \frac{SH}{V_\alpha(\theta_\infty - \theta_c)} = C_h(R_o, S) \quad (3.21)$$

where $C_f(R_o, S)$, $C_h(R_o, S)$, and $\alpha_0(R_o, S)$ have different forms for stable and unstable PBLs. The latent heat flux (LH) is computed by assuming that it obeys

the universal function for SH, that is,

$$\frac{q - q_0}{q_*} = \frac{\theta - \theta_0}{\theta_*} \quad (3.22)$$

where

$$q_* = \frac{-LH}{u_*} \quad (3.23)$$

c. Frictional drag

The frictional effects of the boundary layer are simulated with a simple aerodynamic drag formulation based on Sutton (1953). In the lowest model layer, the frictional term in (2.2) is given by

$$\vec{F}_{uv} = -\frac{\rho}{\pi H} \frac{\partial \vec{\tau}_{xy}}{\partial \eta} \quad (3.24)$$

where the surface stress vector $\vec{\tau}_{xy}$ is given by

$$\vec{\tau}_{xy} = \rho C_d (V_0 u \hat{i} + V_0 v \hat{j}) \quad (3.25)$$

with $C_d = u_*^2 / V_0^2$, and where V_0 represents the magnitude of the wind in the model layer just above the boundary layer.

d. Ground variables

Ground temperature (TG) and ground wetness (GW) are parameterized by "force restore" methods from Bhumralker (1975) and Deardorff (1977). Following Bhumralker (1975), heat conduction in the soil is described by

$$\frac{\partial T_g(z,t)}{\partial t} = \frac{\kappa}{c} \frac{\partial T_g(z,t)}{\partial z^2} \quad (3.26)$$

where $T_g(z,t)$ is the soil temperature at depth z and time t . We assume that TG is described by

$$TG = \bar{T} + \Delta T_0 \sin(\omega t) \quad (3.27)$$

where \bar{T} is the average temperature of the soil, and ΔT_0 is the amplitude of the variance. Then the solution of (3.26) is

$$T_g(z,t) = \bar{T} + \Delta T_0 \exp(-z/d) [\sin(\omega t - z/d)] \quad (3.28)$$

where $d = (2\kappa/c\omega)^{1/2}$ is the depth at which the amplitude of ΔT_0 is negligible. For an infinitely thin soil layer, the heat flux into the soil at depth z is

$$G(z,t) = -\kappa \frac{\partial T_g(z,t)}{\partial z} \quad (3.29)$$

Combining (3.28) and (3.29) gives

$$G(z,t) = \left(\frac{\omega c \kappa}{2}\right)^{1/2} \Delta T_0 e^{-z/d} [\sin(\omega t - z/d) + \cos(\omega t - z/d)] \quad (3.30)$$

Eliminating ΔT_0 one obtains

$$G(z,t) = \left(\frac{\omega c \kappa}{2}\right)^{1/2} \left[\frac{1}{\omega} \frac{\partial T_g(z,t)}{\partial t} + T_g(z,t) - \bar{T} \right] \quad (3.31)$$

Consider a layer of soil from the surface ($z = 0$) to some depth z . The time rate of temperature change for this layer is given by

$$c \frac{\partial T_g(z,t)}{\partial t} = - \left[\frac{G(z,t) - GS}{z} \right] \quad (3.32)$$

If the approximation is made that

$$T_g(z=1 \text{ cm}, t) \approx TG \quad (3.33)$$

then (3.32) becomes [with the use of (3.9)],

$$\left[c + \left(\frac{c\kappa}{2\omega}\right)^{1/2} \right] \frac{\partial TG}{\partial t} = GS - \left(\frac{\omega c \kappa}{2}\right)^{1/2} (TG - \bar{T}) \quad (3.34)$$

or

$$\frac{\partial TG}{\partial t} = \left[GS - \left(\frac{\omega c \kappa}{2}\right)^{1/2} (TG - \bar{T}) \right] \left[c + \left(\frac{c\kappa}{2\omega}\right)^{1/2} \right]^{-1} \quad (3.35)$$

The surface soil moisture (GW) is found by assuming that it changes due to three main processes—precipitation, evaporation, and flux from below. The bulk soil moisture (GWB) is assumed to be constant over the period. According to Deardorff (1977) the bulk soil moisture changes over a time scale of a few weeks, so GWB can be assumed constant for a 24 h period with little loss of accuracy. The surface soil moisture is changed according to

$$\frac{\partial GW}{\partial t} = - \frac{c_1(LH/\lambda - P_r)}{\rho_w d_1 W_{max}} - \frac{c_2(GW - GWB)}{\tau_D} \quad (3.36)$$

Deardorff's values for the nondimensional constants c_1 and c_2 were computed from data of Jackson (1973), which used measurements taken over bare soil near Phoenix, Arizona in March. This gives

$$c_1 = \begin{cases} 0.5 & GW \geq 75\% \\ 14 - 22.5(GW - 0.15) & 15\% < GW < 75\% \\ 14 & GW \leq 15\% \end{cases} \quad (3.37)$$

$$c_2 = 0.9$$

The above discussion of the surface temperature and soil moisture parameterizations applies for grid boxes composed of land. For grid points over water, the value of TG is set to be the temperature of the water and held constant over the integration, and the soil moisture is set to reflect a water surface capable of continual evaporation. Grid boxes composed of a mixture of land and water surfaces should produce fluxes that represent some sort of weighted average between those from all-land boxes and those from all-water boxes. Several schemes using the framework of the above parameterizations were tested to try to make use of knowledge of the land-water mix of the grid boxes, but none of them proved satisfactory for all possible types of conditions. While a weighted-average flux approach seems very straightforward, the coupling of the surface temperature prediction with the incoming and outgoing radiation calculation and the forecast fluxes leads to approximations that cannot be good for both day and night. Other approaches led to similar difficulties.

e. Boundary-layer height

1) Unstable boundary layer

The unstable PBL is assumed to be well mixed below an inversion characterized by a jump discontinuity in potential temperature ($\Delta\theta$). The depth of the unstable boundary layer, h , and the strength of the inversion, $\Delta\theta$, are predicted according to Zeman and Tennekes (1977). Their method assumes that the PBL depth changes due to turbulent entrainment of air above the inversion into the PBL. The energy comes from the virtual SH flux at the surface, and the change of depth with time depends on the strength of the inversion. They use the turbulent kinetic energy (TKE) budget to develop a simple set of equations to describe this process.

The sensible heat flux at the inversion is equal to the temperature jump, $\Delta\theta$, times the rate of rise of the inversion

$$VSH_h = \Delta\theta \frac{\partial h}{\partial t} \quad (3.38)$$

where VSH_h is the virtual sensible heat flux at the inversion. The inversion strength changes as a function of entrainment of stable air from above, and net sensible heat transfer inside the boundary layer. It is given by

$$\frac{\partial \Delta\theta}{\partial t} = \gamma \frac{\partial h}{\partial t} - (VSH - VSH_h)/h \quad (3.39)$$

where VSH is the virtual sensible heat flux at the surface and γ is the potential temperature lapse rate above the PBL. The TKE budget can be written as

$$\frac{\partial(TKE)}{\partial t} = \text{production} + \text{transfer} + \text{dissipation} \quad (3.40)$$

which can be expanded into

$$C_t \frac{w_*^2}{h} \frac{\partial h}{\partial t} = \frac{g}{TS} VSH_h + C_f \frac{w_*}{h} - C_d w_*^2 \omega_{bv} \quad (3.41)$$

where C_t , C_f , and C_d are dimensionless constants. Substituting for $\partial h / \partial t$ from (3.38) yields

$$-\frac{g}{TS} VSH_h = \frac{w_*^3}{h} \left[C_f - C_d \omega_{bv} \left(\frac{h}{w_*} \right) \right] \left[1 + \frac{C_t w_*^2 TS}{g \Delta \theta h} \right]^{-1} \quad (3.42)$$

Substituting for w_* (see appendix A) gives

$$-\frac{VSH_h}{VSH} = \left[C_f - C_d \omega_{bv} \left(\frac{h}{w_*} \right) \right] \left[1 + \frac{C_t w_*^2 TS}{g \Delta \theta h} \right]^{-1} \quad (3.43)$$

The values of the dimensionless coefficients C_d , C_f , and C_t are taken to be (Zeman 1975)

$$\begin{aligned} C_d &= 0.024 \\ C_f &= 0.50 \\ C_t &= 3.55 \end{aligned} \quad (3.44)$$

We can write the rate of change of boundary layer height as

$$\frac{\partial h}{\partial t} = - \frac{VSH_h}{\Delta \theta} \quad (3.45)$$

In the case where $\Delta \theta = 0$, no inversion exists and the atmosphere presents no barrier to inversion rise. In this case, the model assumes a very small value for $\Delta \theta$, since the inversion must rise at a rapid but finite rate due to turbulent entrainment.

2) Stable boundary layer

The depth of the stable boundary layer is calculated using a parameterization from Zeman (1979). The mean kinetic energy budget is the basis for a rate equation governing the height of the stable boundary layer. This results in

$$\frac{dh}{dt} = \frac{3}{2} u_* \left[\frac{C_F^*}{(1 + 5h/L)} - \frac{2}{3} \frac{u_*}{|\Delta \mathbf{u}|^2} (\Delta u \cos \xi + \Delta v \sin \xi) \right] + \frac{h \Delta \mathbf{u}}{|\Delta \mathbf{u}|^2} \cdot \frac{\partial \mathbf{V}_0}{\partial t} \quad (3.46)$$

where the quantity C_F^* is a tunable function of the Richardson number, determined by comparison with numerical and laboratory results, and ξ is the angle between the geostrophic wind above the boundary layer and the surface stress.

f. Boundary-layer variables

The surface temperature is found as a by-product of the PBL depth calculations. For the unstable PBL, we proceed as follows:

$$\Delta\theta_P = \theta_i + \frac{z_t - \Delta h}{z_t} (\theta_P - \theta_i) - \theta_P \quad (3.47)$$

where Δh is the change in PBL depth over one time step.

The potential temperature at the top of the 5 mb surface layer is given by

$$\theta_s = \theta_P - \Delta\theta \quad (3.48)$$

which allows the surface temperature to be found by Poisson's equation as

$$TS = \theta_s \left[\frac{p_{sfc} - 5}{1000} \right]^{0.286} \quad (3.49)$$

For the stable PBL, we start in a similar manner but that there is no inversion jump discontinuity. We simply interpolate in potential temperature between the PBL top and the ground to find θ_s then compute TS with (3.49).

g. Boundary-layer transitions

Transitions between stable and unstable boundary-layer regimes have been incorporated into the boundary-layer parameterization. In the real atmosphere, these transitions are almost certainly abrupt and characterized by poorly defined structures. Within the model, such a situation would lead to numerical problems. In addition, there is no known parameterization for a boundary layer in transition, so we have to provide a mechanism for an orderly transition.

The transition stage is determined by the sign of the sensible heat flux. When the direction of the sensible heat flux is incompatible with the nature of the boundary layer, the transition stage is set. The boundary-layer height is constrained to fall rapidly from its current location to a height of 90 m (arbitrarily chosen). To do this, the boundary-layer height tendency is initially set at a value that would cause the boundary layer to be 90 m after 15 min. The tendency is

adjusted each time step according to

$$\frac{dh}{dt} = \left[\frac{dh}{dt} \right]_{old} \left[\frac{h - 90}{90} \right]^{\frac{1}{2}} - (6 \text{ m min}^{-1}) \quad (3.50)$$

where the subscript "old" refers to the previous timestep. The multiplicative factor slows the rate of change as the transition nears completion while the 6 m min⁻¹ additive constant assures that the transition will be completed in a finite time. During this transition, the potential temperature structure in the boundary layer is changed as little as possible, thereby allowing the proper parameterization to begin with the current structure as though the transition had been instantaneous. The potential temperature at the top of the boundary layer is linearly interpolated between its current value and the potential temperature of the ground. Boundary-layer moisture is conserved during this process of boundary-layer height fall, again to preserve current conditions as much as possible. When the boundary-layer height reaches 90 m the transition ends. The boundary layer then begins to grow again according to the stability at that time.

Transitions from unstable to stable and vice versa have been tested and found to be relatively smooth and reliable. Although most of these transitions will take place at dawn or dusk, it is conceivable that a major change in cloud cover or air mass might initiate such a change at any time during an integration. The only aspect of this that will not be handled well by the parameterization is a situation in which a well-mixed convective boundary layer grows to a substantial depth, then the radiation is interrupted by clouds, causing a transition to a stable boundary layer, followed by a breakup of the clouds and a return to unstable stratification. The new convective boundary layer will start over and the atmosphere above the boundary layer, which in the real atmosphere would be almost dry adiabatic in structure, will be slightly stable in the model. This is, of course, a problem with the limited vertical resolution of the model, not the fault of the parameterization. Only extensive testing will be able to show if this is a serious problem. We suspect that most cloud cover will only reduce the sensible heat flux in magnitude rather than actually reversing the sign. Hence, the boundary layer will grow much more slowly but will not go through a transition.

4. Simulations with the model

a. *Mountain lee-wave simulations*

A critical test of any meso- β scale model is the simulation of mountain lee-waves (Anthes and Warner 1978; Nickerson et al. 1986). While previous investigators have usually made these tests with a two-dimensional version of their models (Anthes and Warner 1978; Nickerson et al. 1986), we choose to use the full three-dimensional model—except without any boundary layer or radiation parameterizations. By choosing a long uniform ridge oriented perpendicular to the flow, we can obtain a nearly two-dimensional solution crossing the center of the ridge (which allows comparison with previous two-dimensional simulations), while not modifying the three-dimensional staggering of the variables as required in a two-dimensional analog model. Since the boundary-layer parameterization is turned off for this test, the boundary-layer height must be specified and is held constant. While many boundary-layer heights were tested, including artificially varying ones, we will show the results when $\sigma_h = 0.80$ which represents equally spaced layers for the model.

For the simulation discussed in this section, the thermodynamic profile was specified as the U. S. Standard Atmosphere, the specific humidity was set to zero, and the u -component winds were specified as 20 m s^{-1} at all levels. The Coriolis force is included in the model for these simulations, and the initial conditions were in approximate geostrophic balance (at a latitude of about 40°N). A mountain ridge with Gaussian cross section and a maximum elevation of 1 km was oriented north-south near the center of the FGM domain. The ridge had a constant height for the center 12 north-south grid points and decreased linearly to zero height so that it did not extend into the CGM collar. This avoided problems associated with the specification of the solution on the CGM lateral boundary. Though not presented below, simulations with the ridge rotated 90° and with winds from the south, north, and west were carried out to isolate any coding errors.

Figure 4 shows a vertical cross section through the FGM domain after 12 h simulated time. The isentropic cross section shows the expected lee-wave structure with the waves sloping upstream with height; this is also reflected in the horizontal velocity field. While the isentropes in Fig. 4 are plotted objectively by linear

interpolation, the isotachs are subjectively analyzed because of the coarse vertical resolution. These results are quite similar to those obtained for similar conditions by Nickerson et al. (1986) using a model with 16 layers, and by Anthes and Warner (1978) using a model with only 6 layers. It should be noted that Anthes and Warner (1978) discussed the requirement of a relatively large horizontal diffusion in order for a model with few layers and no explicit damping region near the upper boundary to represent lee-waves successfully. As discussed above, the value of K used here leads to a nondimensional diffusion parameter that meets the criteria established by Anthes and Warner (1978).

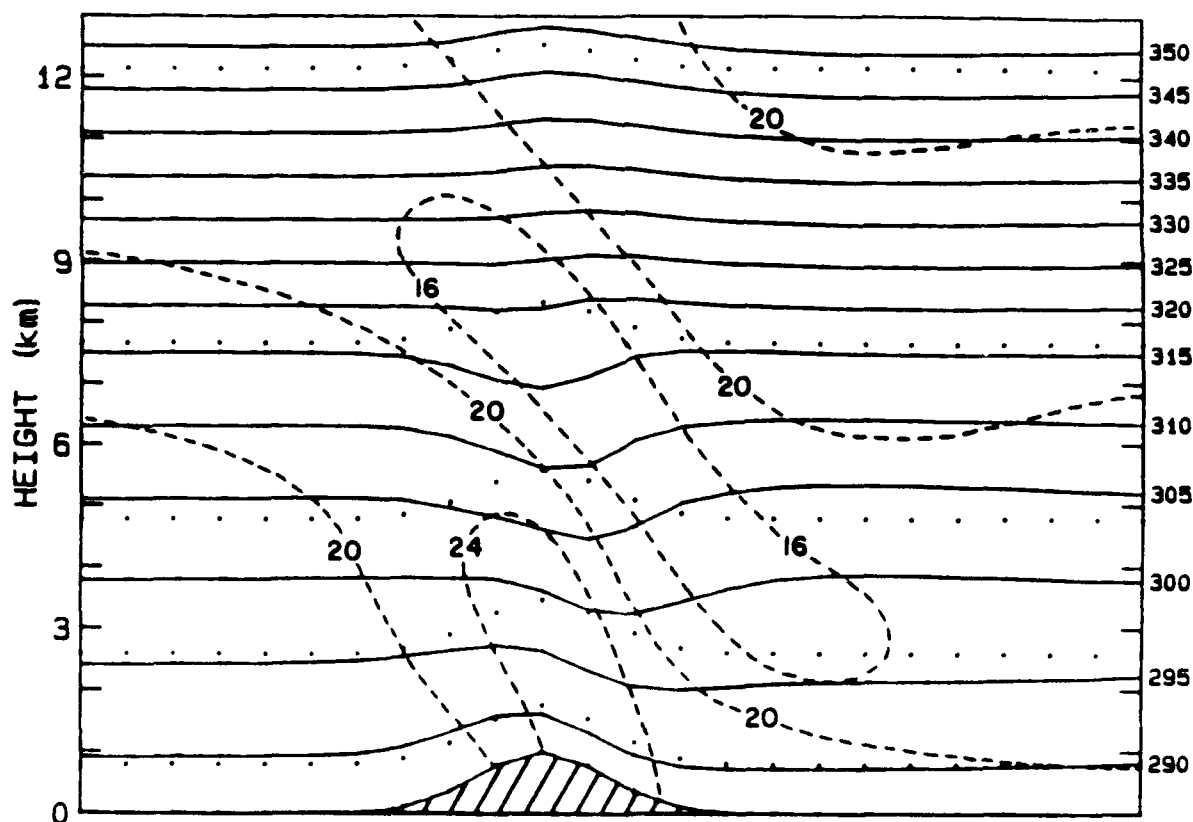
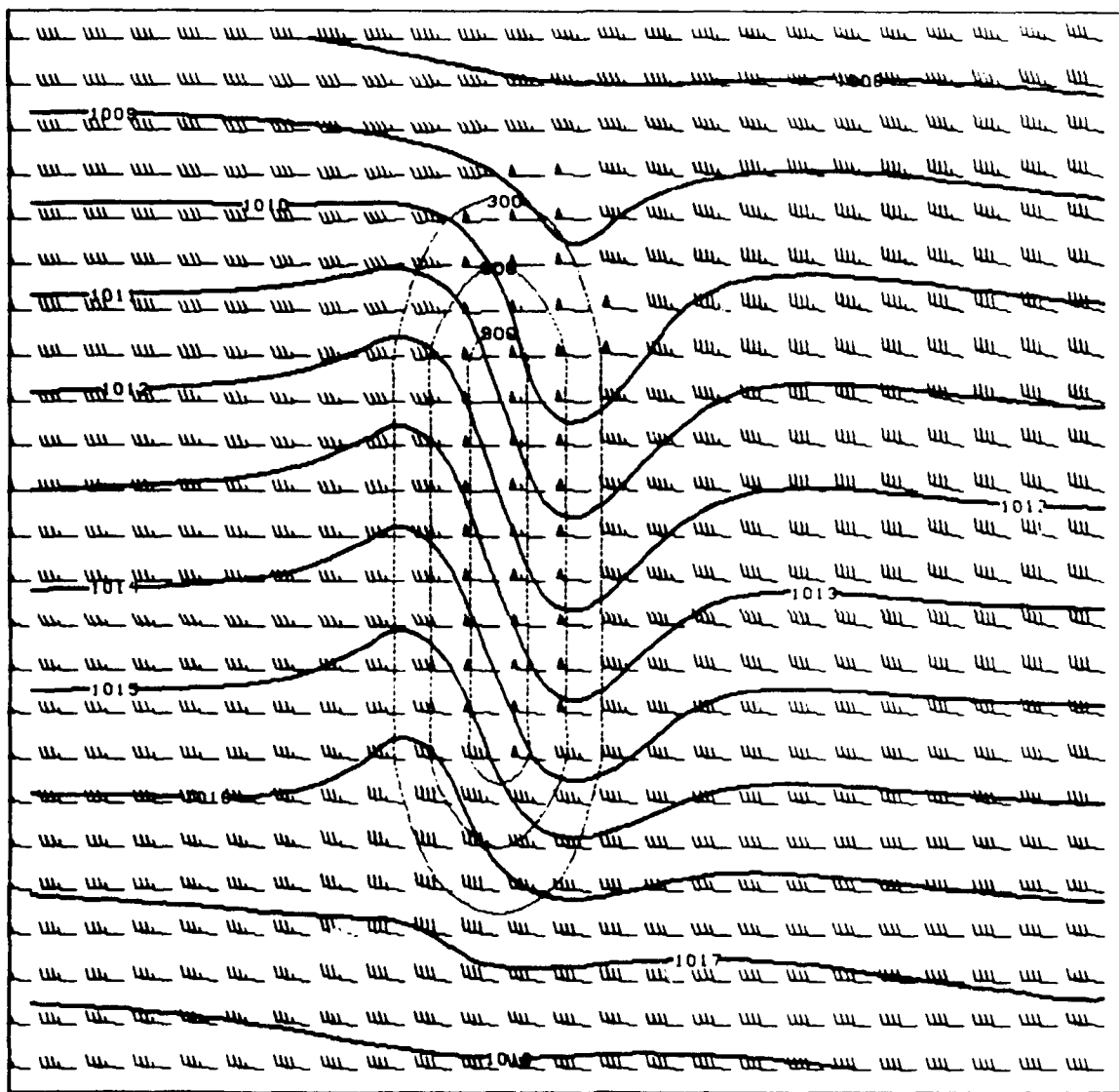


Fig. 4. Vertical cross section through the FGM domain at 12 h simulated time for lee wave simulation showing the potential temperature (solid), and the u -component velocity (dashed). Isentropes are labeled in K along the right and the velocity is contoured in m s^{-1} .



VECTOR WINDS

SURFACE PRESSURE (MB)

SURFACE ELEVATION (M)

Fig. 5. Horizontal plot for simulation shown in Fig. 3. Solid contours give sea-level pressure (in mb), thin dashed contours are for surface topography (in m) of the mountain ridge, and boundary layer winds (one full barb represents 5 m s^{-1}) are plotted at each grid point.

Figure 5 shows a plot of the surface pressure field and boundary-layer winds for this simulation at 12 h simulated time. This figure shows a lee trough and upstream flow blocking that is often associated with flow over a ridge. It is quite evident that the model solution is smooth and well-behaved, even at the lateral boundaries representing the FGM/CGM interface. Figure 6 shows the average rate of change of surface pressure in the FGM during the integration. It is clear that the model undergoes an adjustment during the first few hours of integration as the pressure adjusts to the mountain lee-wave structure. The model is quite steady for the last 6 hours of the integration, a fact confirmed by plots (not shown) of winds and surface pressure at 8 h and 10 h.

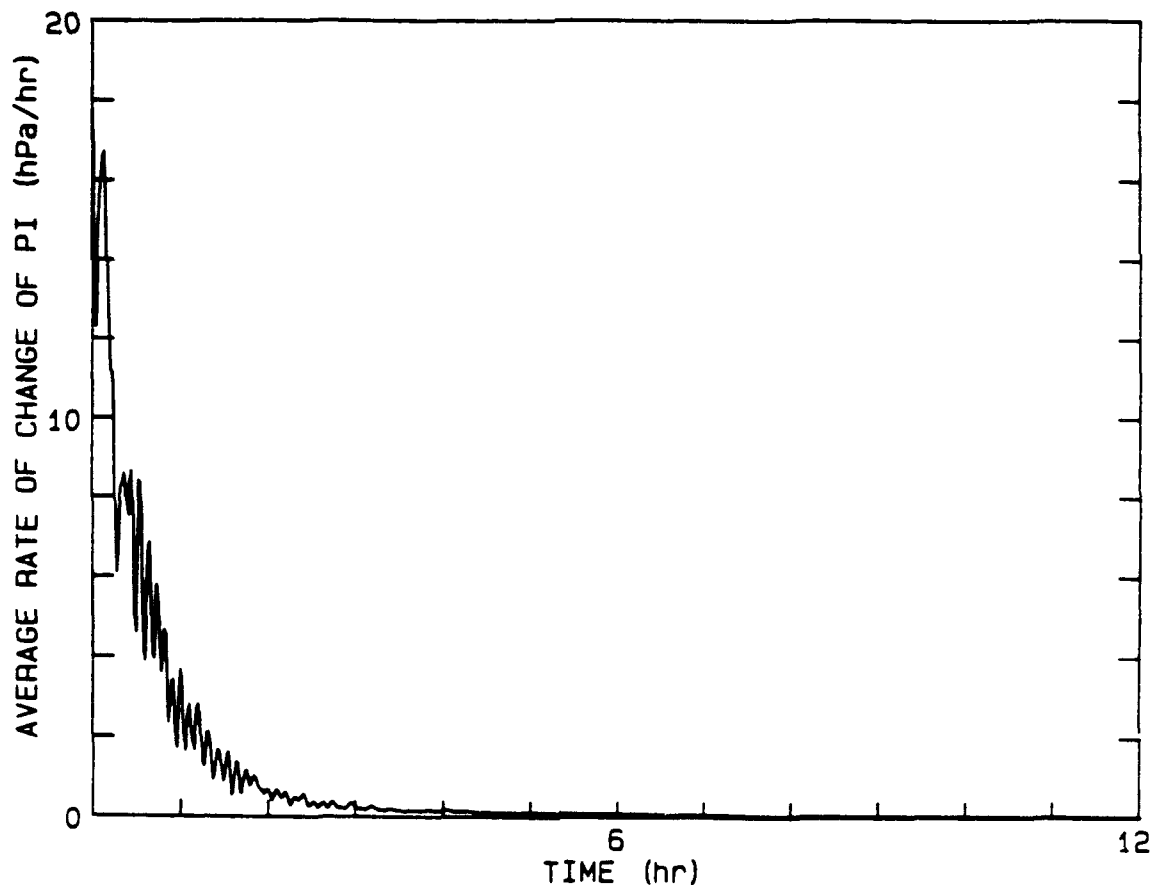


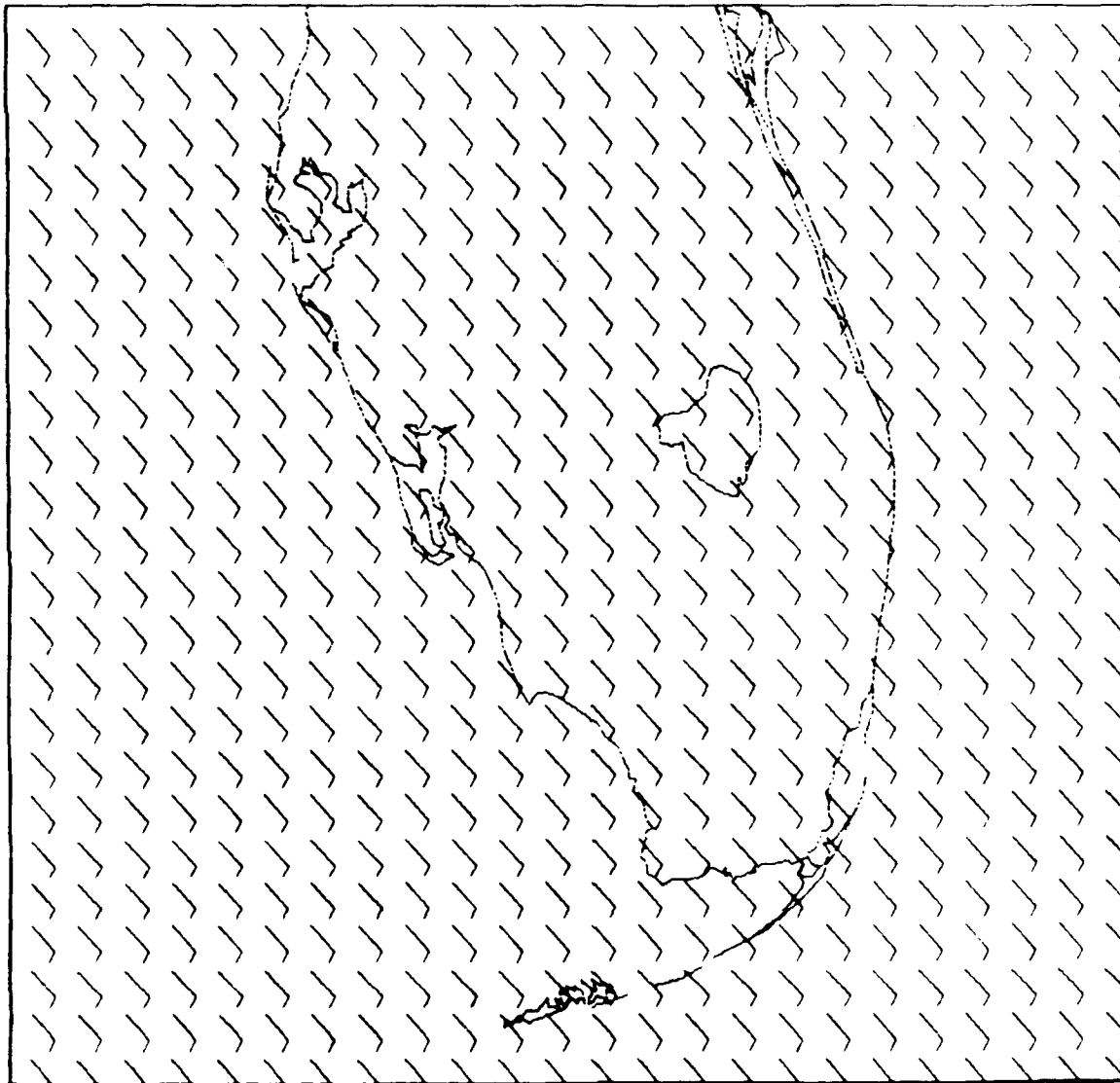
Fig. 6. Average rate of change of π versus time for FGM domain during the simulation shown in Figs. 4 and 5.

Although written in the framework of boundary-layer coordinates, the model reduces to a traditional σ -coordinate model if the boundary-layer height, σ_h , is specified as a constant in the domain—as it was in the simulation discussed above. Numerous simulations in which the boundary-layer height was artificially raised or lowered were carried out for the mountain lee-wave case. Even when the boundary-layer height was changing relatively rapidly, the lee-wave structure was preserved and the model maintained a near geostrophic balance for pressure and wind fields (Colby and Seitter 1990).

b. Sea-breeze simulation

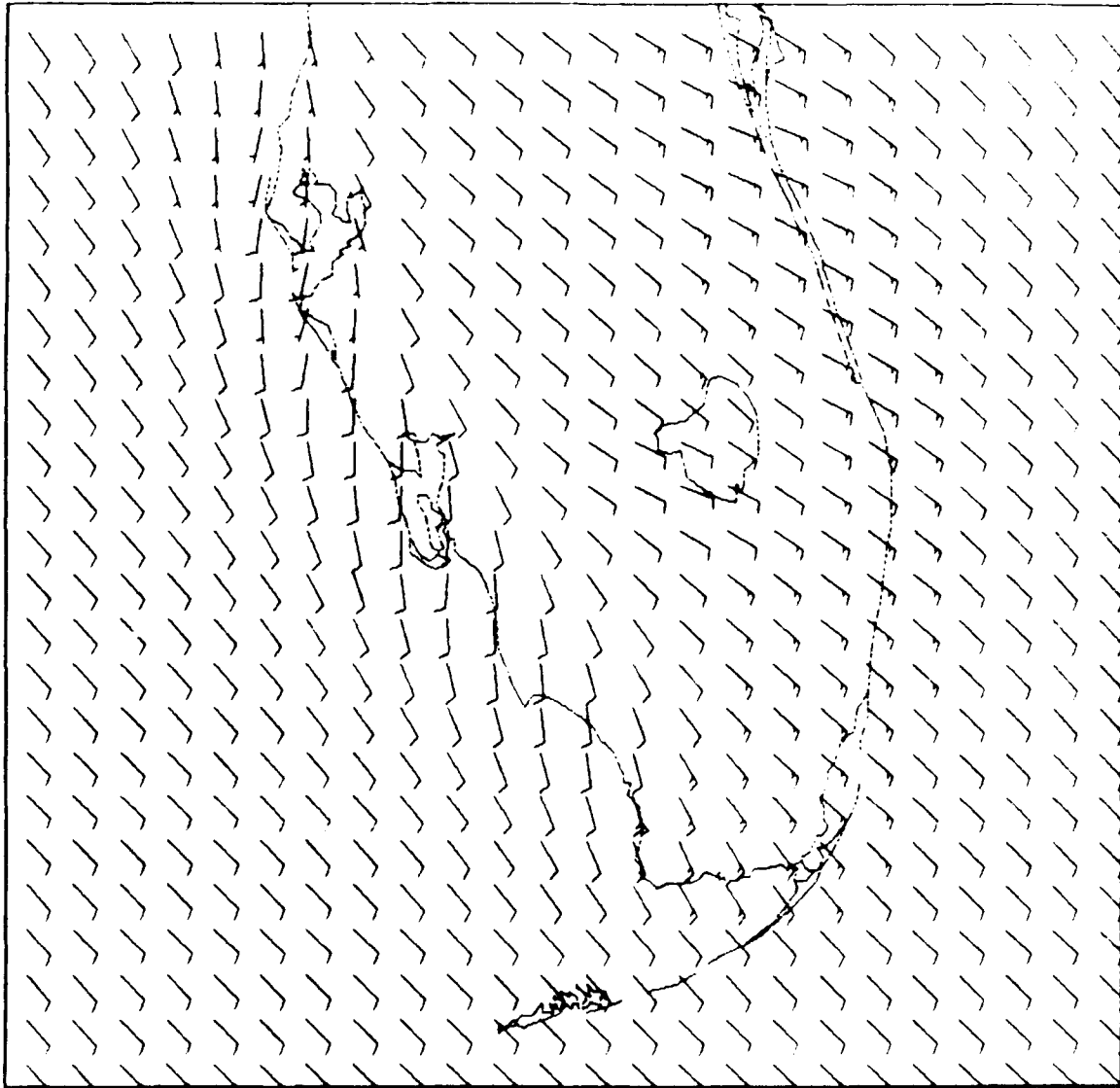
The full capabilities of the boundary-layer coordinate system can only be tested if a mesoscale circulation that depends on boundary-layer processes is simulated. A natural candidate for such a test is a sea-breeze circulation. In order to isolate boundary-layer processes from topographic forcing, we choose to simulate the sea-breeze circulation of southern Florida, which we treat as a flat land mass at zero elevation. We will show here a simulation similar to the "southeast flow" case treated by Pielke (1972), which matched his initial conditions as much as possible. This included specifying a relatively stable environment [using the Pielke (1972) sounding] and a 7 m s^{-1} synoptic wind from 135° for all levels that was in approximate geostrophic balance with the initial pressure field. The FGM domain with the initialized boundary-layer winds is shown in Fig. 7. The head of each wind vector represents the center of a thermodynamic gridbox in the FGM. There are four gridpoints in Lake Okeechobee which are specified as water points in the model. The model simulation is started at 0500 local time on Julian day 180 (01 June), so the simulation begins about one hour before sunrise. Soil moisture content is set uniformly on all land grid points as 50%, and the surface roughness length is set on land and water as 0.04 m and 0.005 m, respectively. The initial boundary-layer height is specified as $\sigma_h = 0.96$ over the entire FGM and CGM domain, which translates to a boundary-layer depth of about 320 m. This simulation is not meant to reproduce a specific observation of the Florida sea-breeze, but the conditions are representative of a class of synoptic situations that leads to an inland convergence zone over the Florida peninsula (Pielke 1972).

Figures 8–10 show the boundary-layer winds in the FGM domain at 6 h, 8 h, and 10 h. The major features of the mesoscale structure are quite similar to those



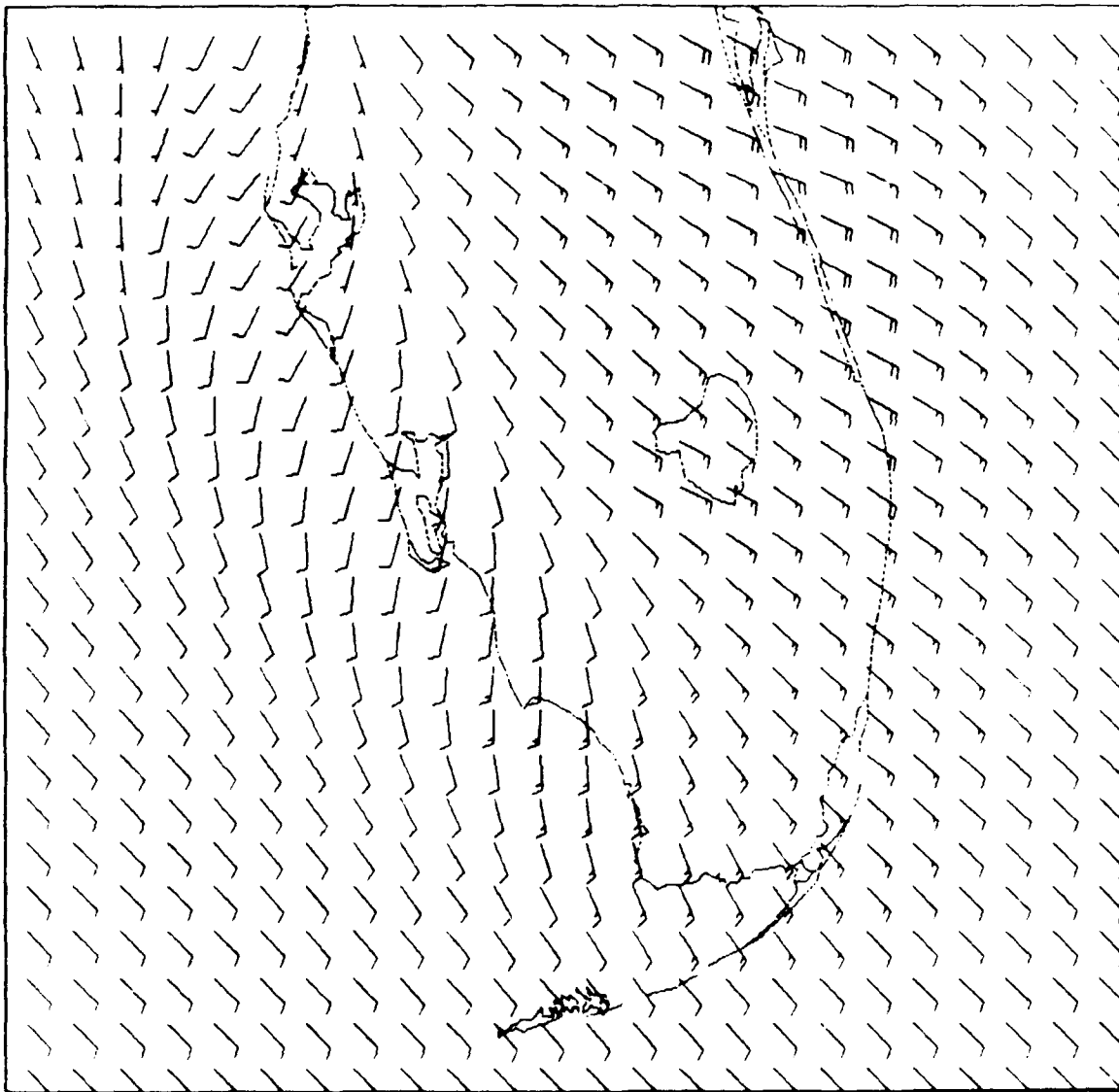
VECTOR WINDS

Fig. 7. FGM domain and initial boundary-layer winds for Florida sea-breeze simulation.



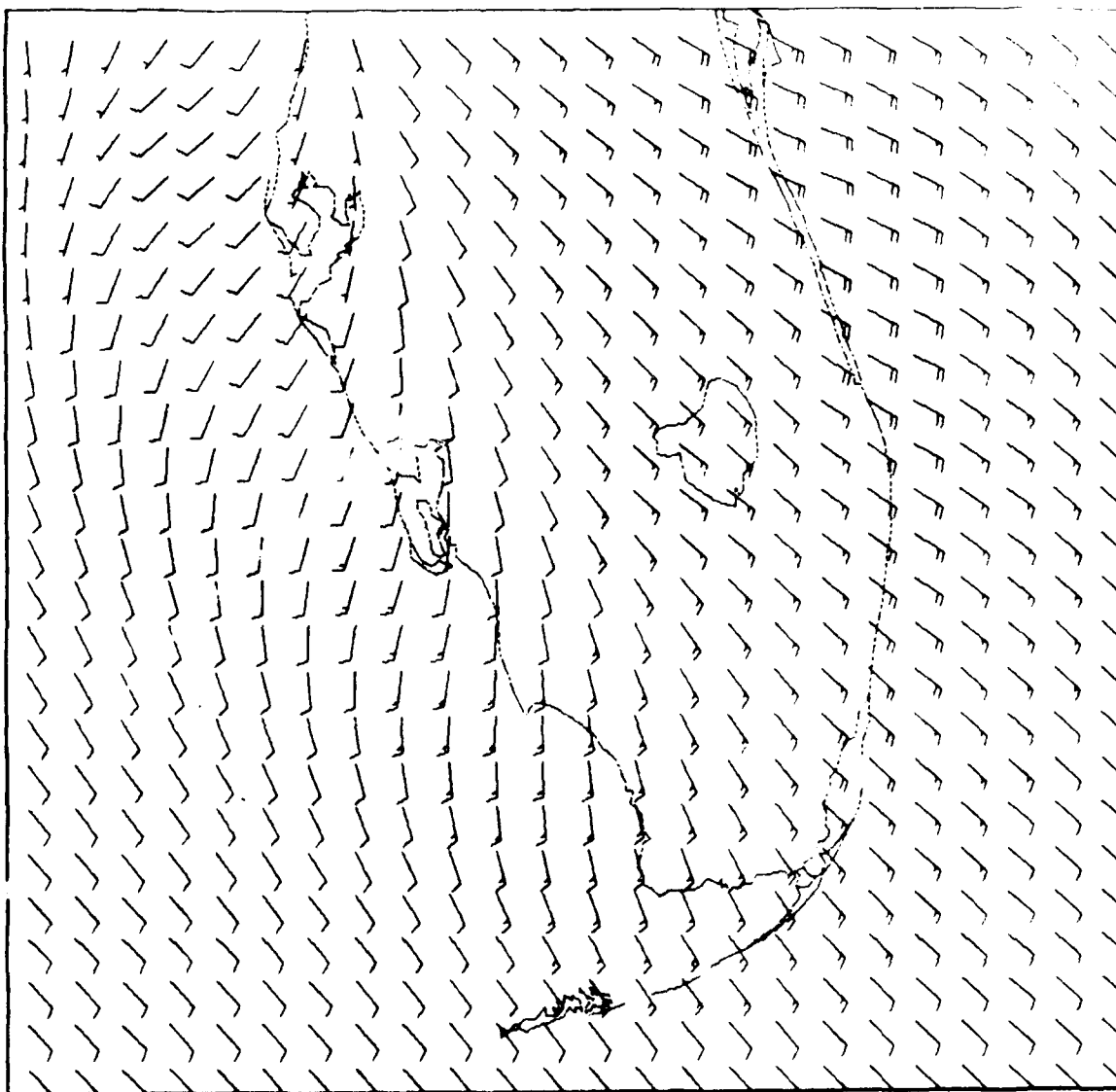
VECTOR WINDS

Fig. 8. FGM boundary layer winds at 6 h, for the Florida sea-breeze simulation.



VECTOR WINDS

Fig. 9. FGM boundary layer winds at 8 h, for the Florida sea-breeze simulation.



VECTOR WINDS

Fig. 10. FGM boundary layer winds at 10 h, for the Florida sea-breeze simulation.

presented by Pielke (1972). The sea-breeze initiated on the western coast must work against the synoptic scale flow while the sea-breeze circulation on the eastern coast simply augments the southeasterly flow and turns it somewhat. A convergence line is established near the western coast. While the 20 km resolution of the present model is not capable of reproducing the complicated wake-like structure downstream of Lake Okeechobee simulated by Pielke's 10 km resolution model, there is clear modification of the flow by the weaker lake-breeze in that region.

An east-west vertical cross-section through the model at 9 h simulated time is shown in Fig. 11. This cross-section was taken at grid row 15, which passes through the center of Lake Okeechobee. The boundary-layer height, denoted by the thin dashed line, is quite high over the warm land regions due to growth as an unstable boundary layer. The boundary layer remains stable and low over the water surfaces, which are much cooler than the land at this time. The temperature gradient near the eastern coast is weaker than that near the western coast because cooler air is advecting in from the east and being warmed by surface heat fluxes from the land. At the western coast, where the sea-breeze circulation is just able to overcome the synoptic winds, there is little advection so a large gradient is established between the cool marine air and the warm air over the land. The structure of the boundary layer in the vicinity of the coast is very similar to that produced by Anthes (1978) with a model utilizing many layers near the surface in order to resolve explicitly the boundary layer changes during the development of the sea-breeze. Despite the large gradients in the boundary-layer height near the coast, very little noise is generated. This is a result of the well-posedness of the boundary-layer coordinate system and the horizontal diffusion operating on the variables.

Figure 12 shows the boundary layer winds in the FGM at 24 h. After sunset, the boundary layer undergoes transition to a stable boundary layer, and as the temperature difference between the land and water decreases, the winds over the whole domain tend to evolve back to the initial southeasterly flow. The synoptic flow over the ocean has, by this time, turned to be somewhat more easterly. This turning toward lower pressure occurs over the course of the integration as the boundary-layer winds over the ocean establish a new balance from the geostrophic initial conditions to one that includes friction. This is not evident in the northern

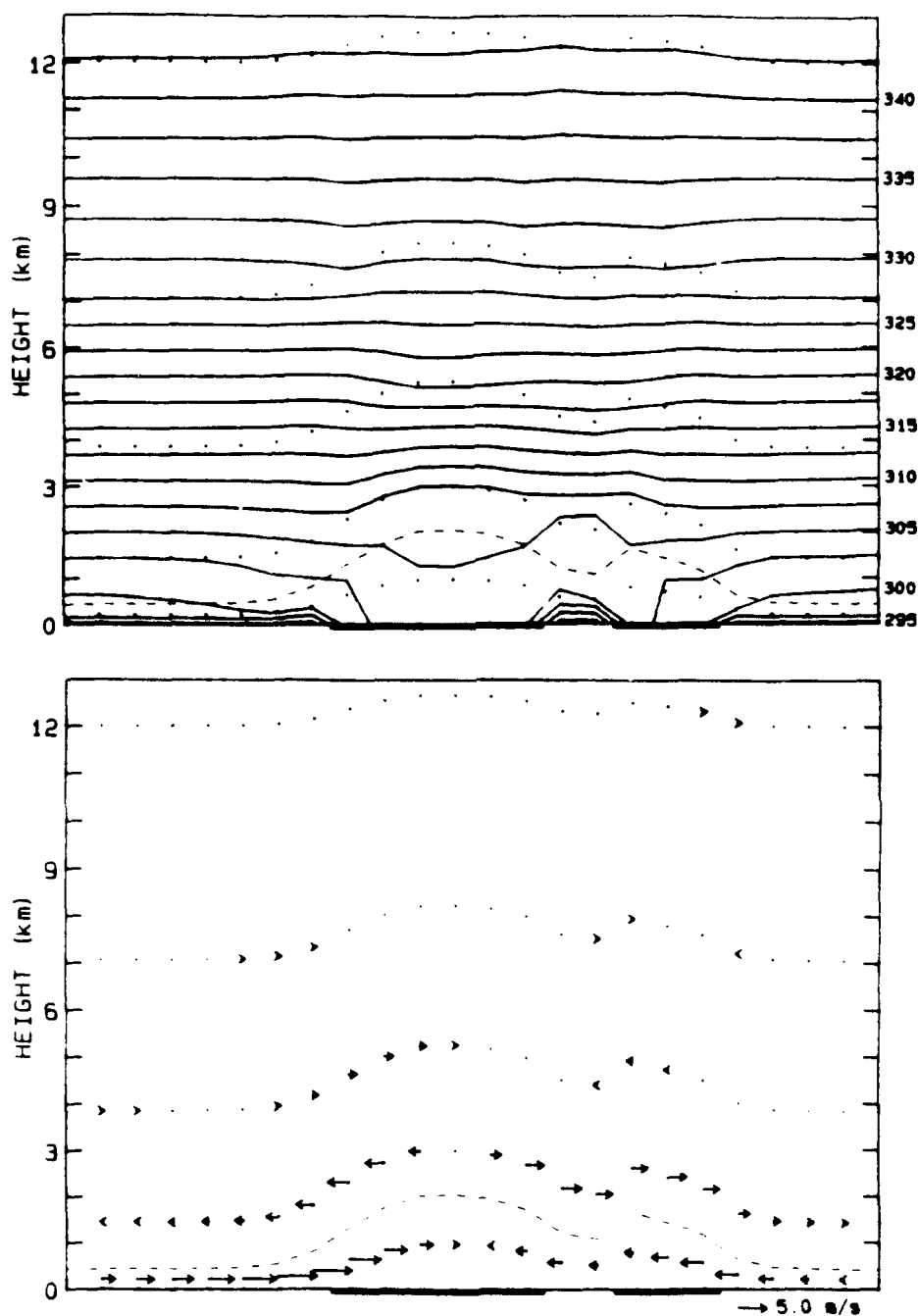
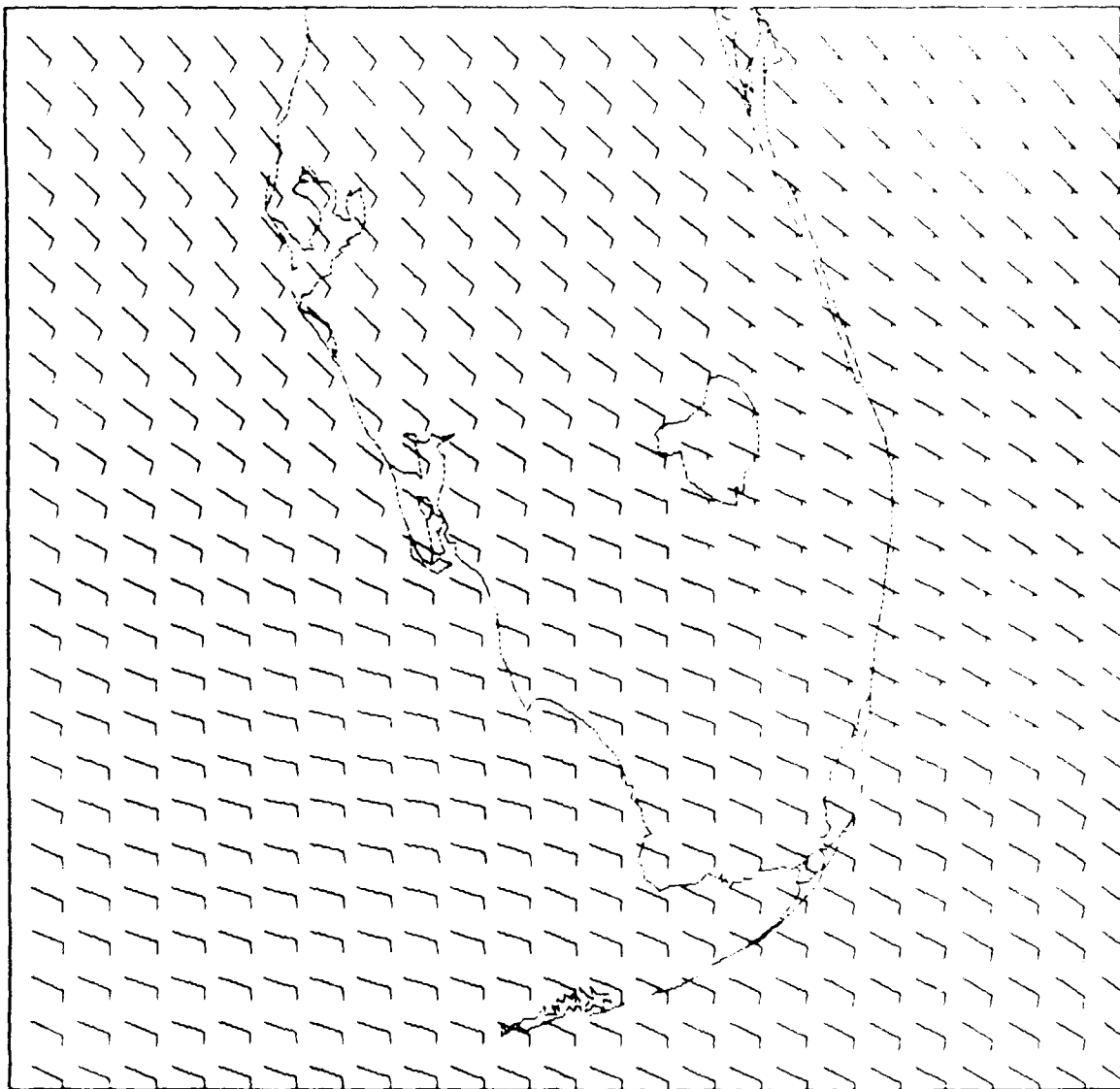


Fig. 11. East-west vertical cross section through the FGM domain at 9 h simulated time for Florida sea-breeze simulation showing (a) the potential temperature, and (b) the u -component perturbation velocity (the synoptic scale u -component has been subtracted out). Isentropes are labeled in K along the right in (a) and velocities are plotted in (b) as arrows whose length is proportional to the magnitude. The top of the boundary layer is shown in (a) by a thin dashed line. Land grid points are indicated by the thick line on the lower boundary.



VECTOR WINDS

Fig. 12. FGM boundary layer winds at 24 h, for the Florida sea-breeze simulation.

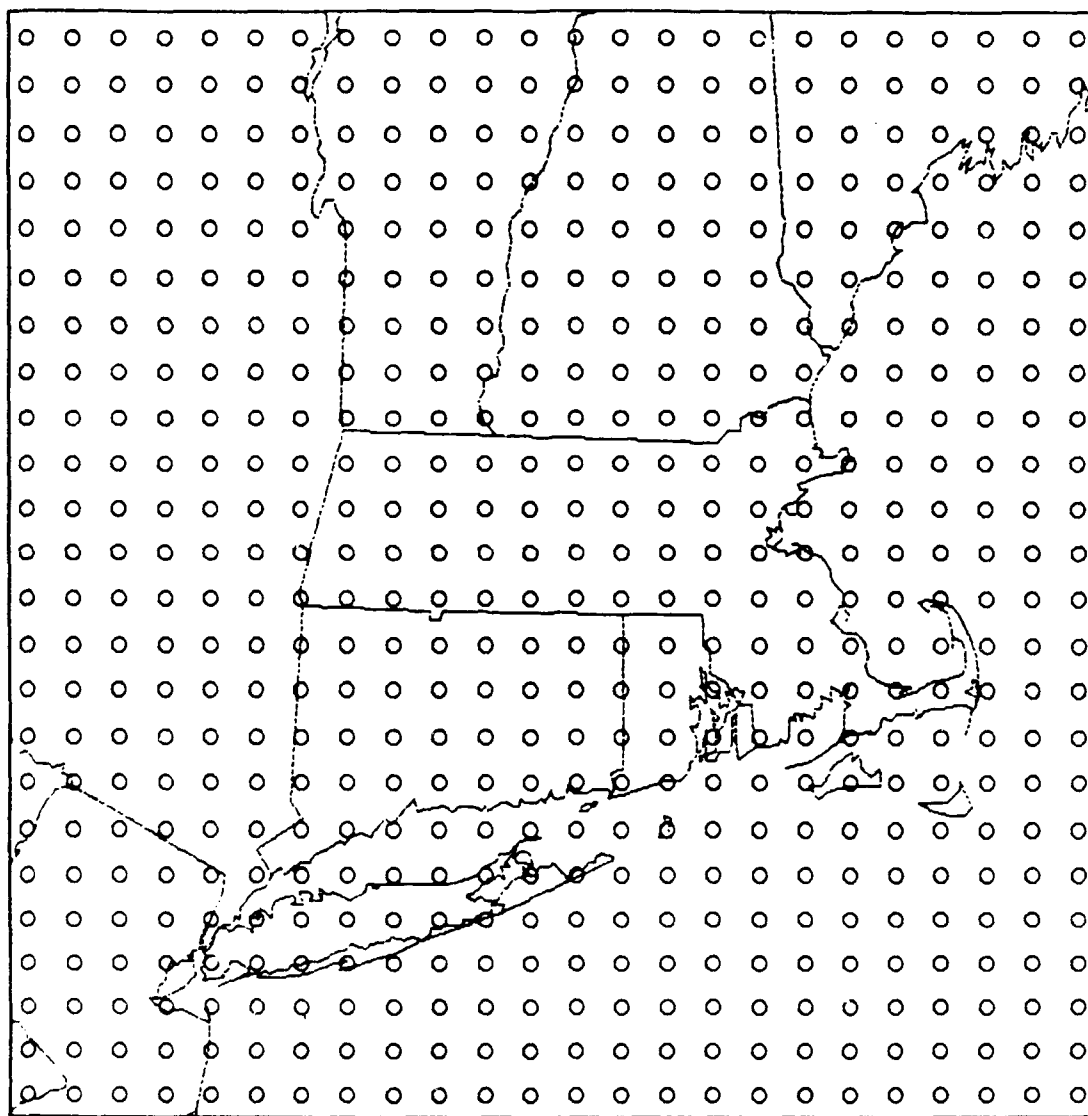
portion of the FGM domain over the oceans because a substantial portion of the northern CGM collar included land and the sea-breeze circulation established there had a large impact on the CGM influence on the FGM winds. The land has cooled radiatively during the night hours and at this time is slightly cooler than the ocean surface—leading to a slight land breeze evident in Fig. 12 as reduced velocity flow on the eastern coastal region. There is also some evidence in the model results to suggest that the reduction of easterly component in the eastern part of the domain is a result of eastward momentum that remained in the boundary-layer flow from the west coast sea-breeze and propagated across the peninsula. The stable boundary layer over land at this time has a height of about 160 m.

5. Initial tests using realistic complex terrain

a. Test domain

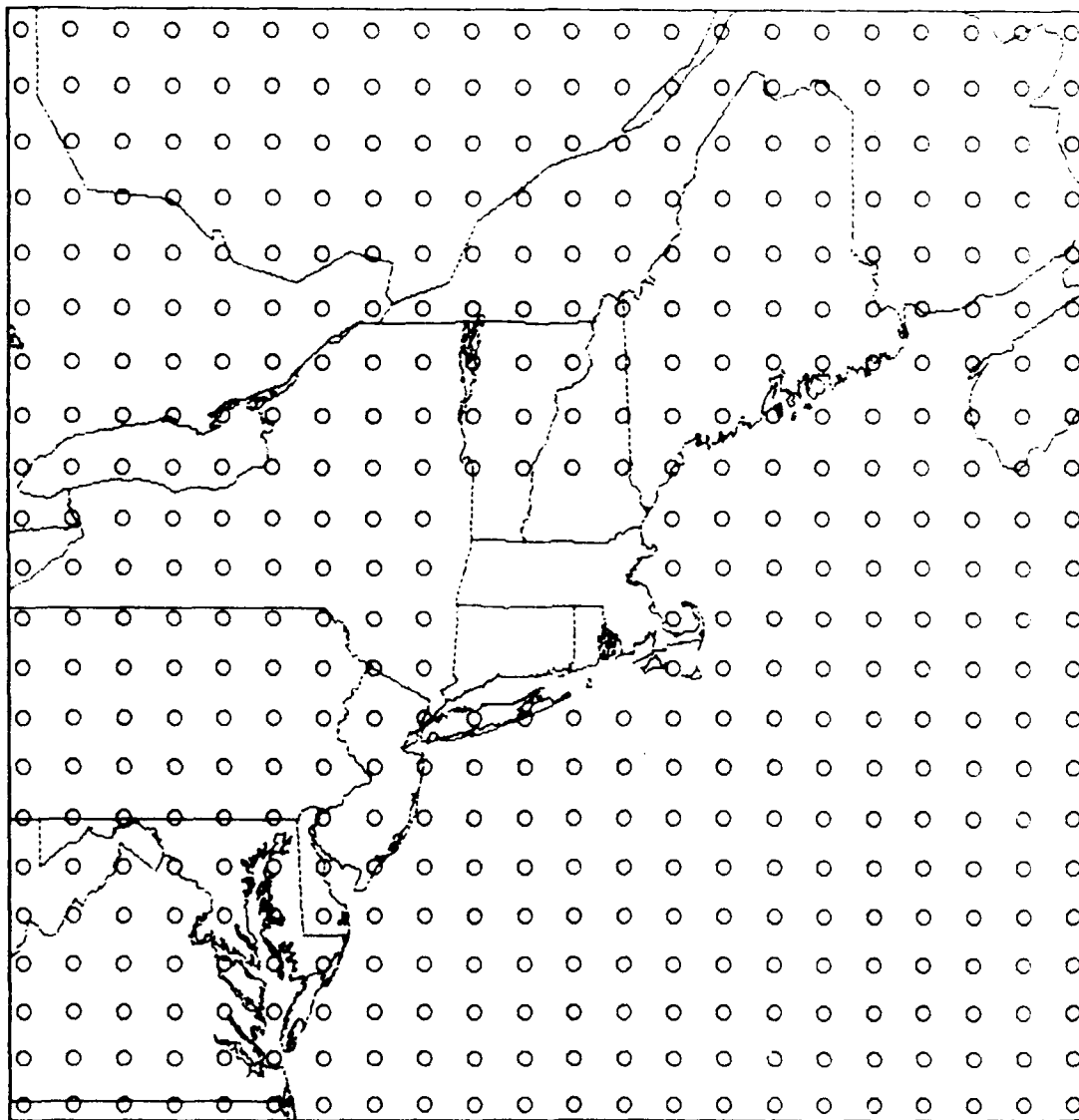
Future research will involve the testing of a prototype model using real data in clear weather and stratiform precipitation situations. Such testing requires a specific geographic location. Ideally, this location should experience a wide variety of weather phenomena such as sea-breeze circulations, synoptic scale stratiform precipitations events, orographic enhancement of precipitation, and other mesoscale patterns for which the model is intended to provide guidance. Southern New England represents one of several locations that could be considered, and given our obvious desire for operational guidance in our own area, we have chosen this geographic region for testing of the prototype model.

The domain for the fine grid mesh is shown in Fig. 13 (only the locations of "thermodynamic" grid points are shown). The coarse grid mesh which surrounds the FGM domain is shown in Fig. 14. In addition to being a coastal location, this area has complex terrain that is rich in detail on meso- β scales. This is quite evident in the contour plot of the FGM topography shown in Fig. 15. The procedure followed to create the partial-envelope orography displayed in this figure is described in detail in appendix C. Several mesoscale orographic features thought to be important to the weather in the New England area are obvious. These include the Adirondack mountains, the Hudson River Valley, the Green Mountains, the Berkshires, the Connecticut River Valley, the White Mountains, and the Worcester



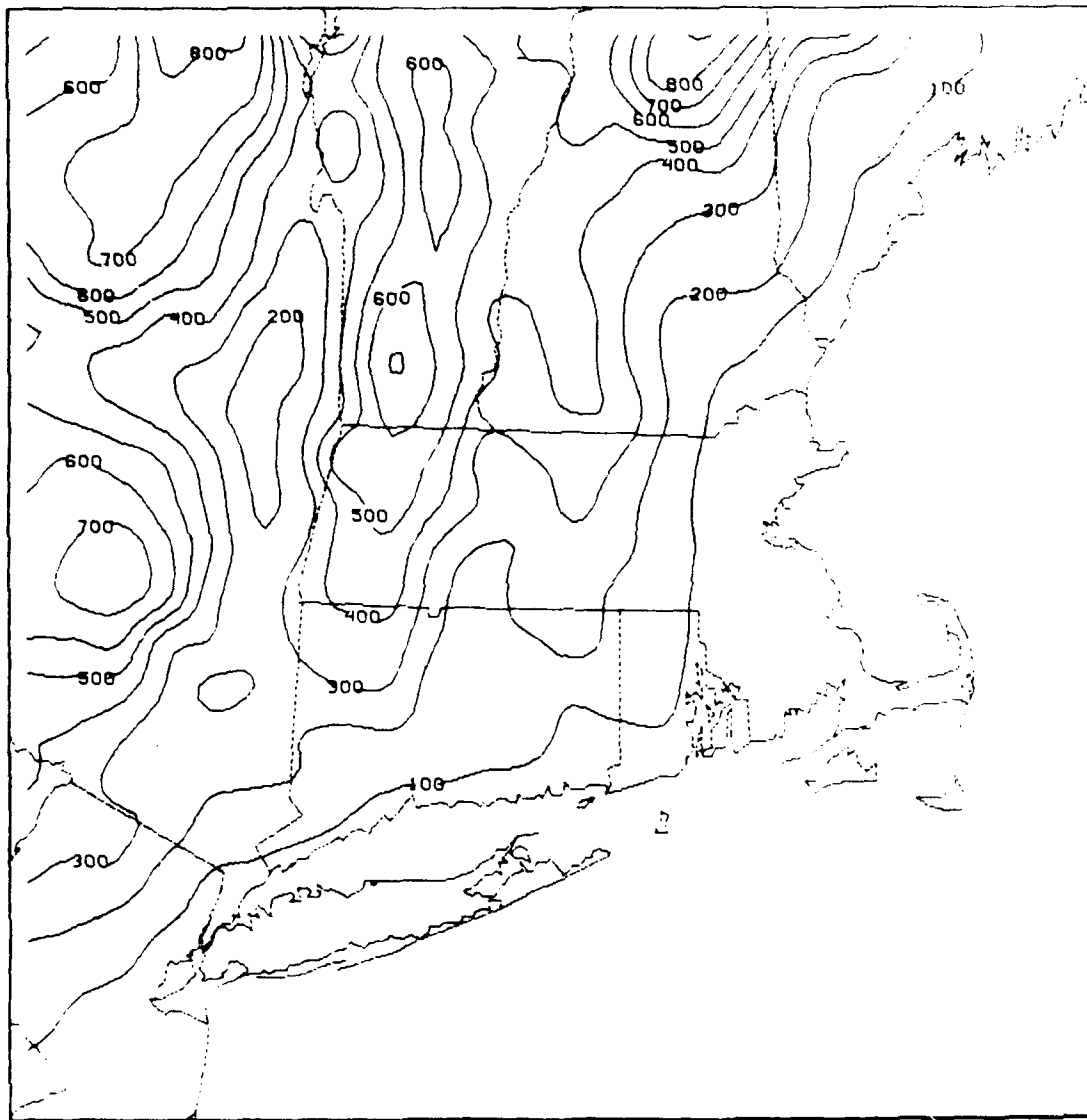
FINE GRID MESH DOMAIN

Fig. 13. FGM domain for New England test simulations showing the location of thermodynamic points.



COARSE GRID MESH DOMAIN

Fig. 14. CGM domain for New England test simulations showing the location of thermodynamic points.



SURFACE ELEVATION (M)

Fig. 15. FGM terrain field (see appendix C for details on the creation of this partial envelope terrain field).

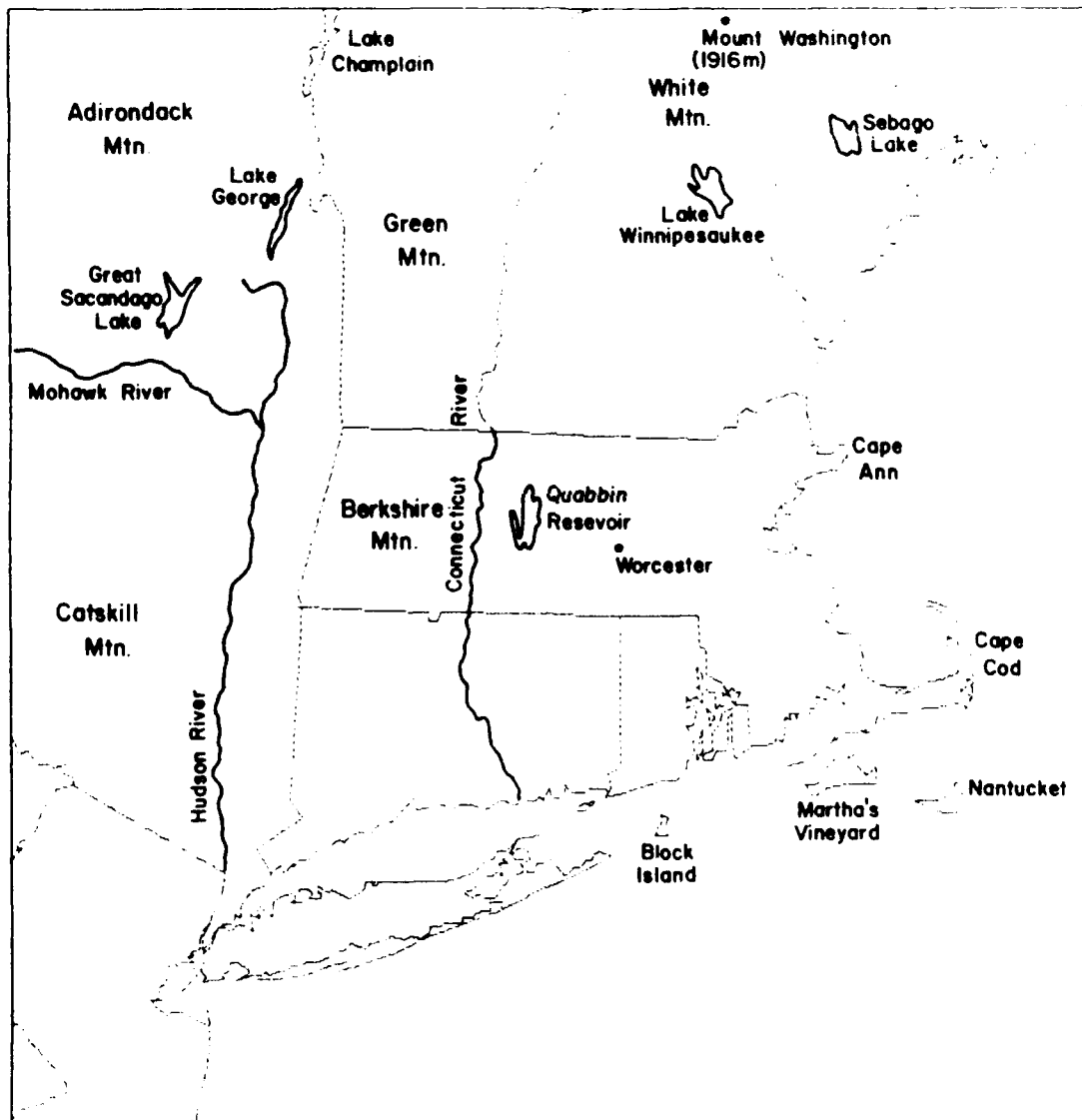
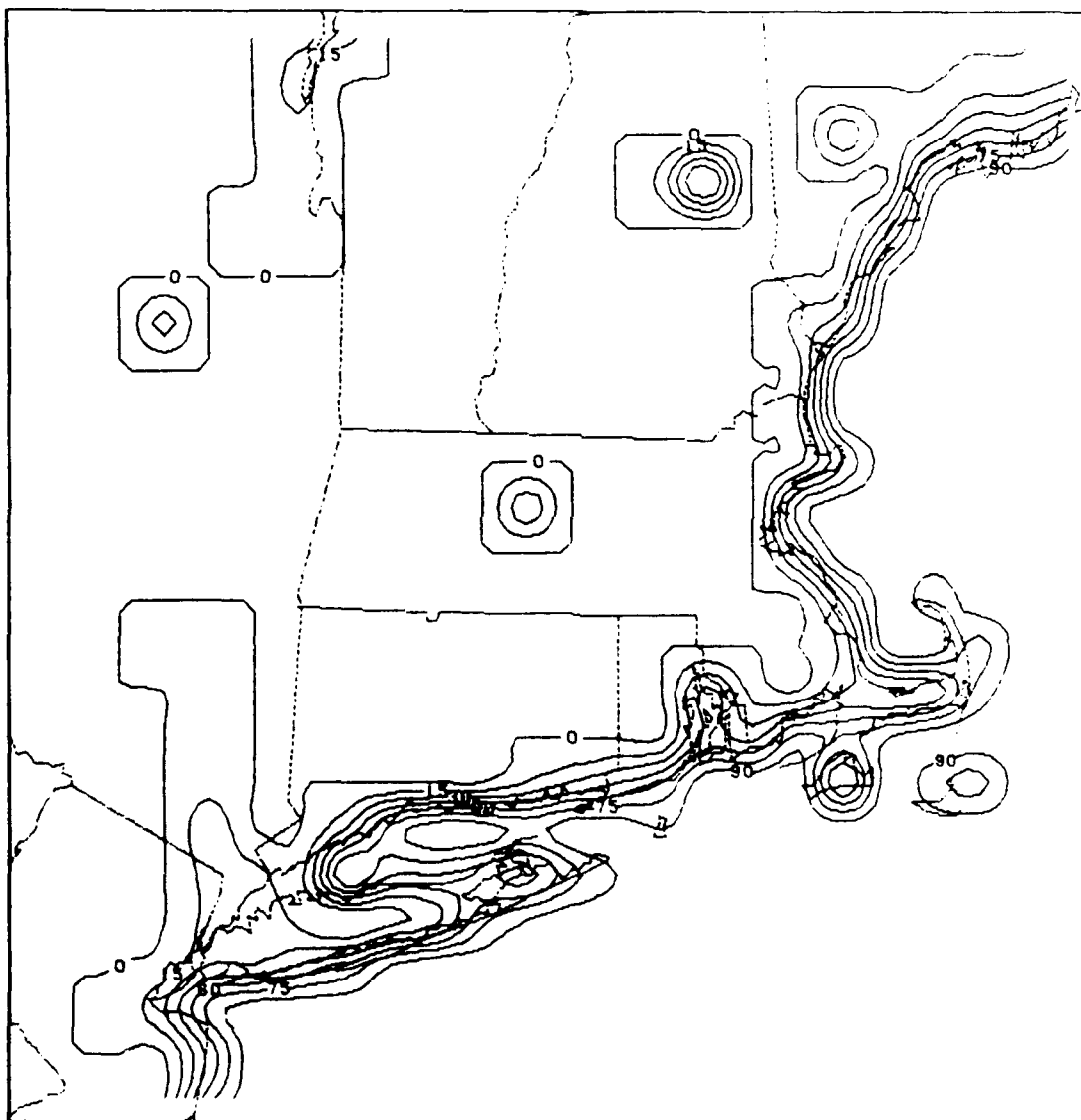


Fig. 16. Map of FGM domain showing major geographic features.

Plateau (see Fig. 16 for a map showing the locations of these features). A potential problem is that Mt. Washington falls almost directly on a grid point at the northern edge of the FGM domain and therefore tends to dominate the terrain field in northern New Hampshire. This particular point may need to be reduced in height in order to avoid numerical problems near the FGM boundary.

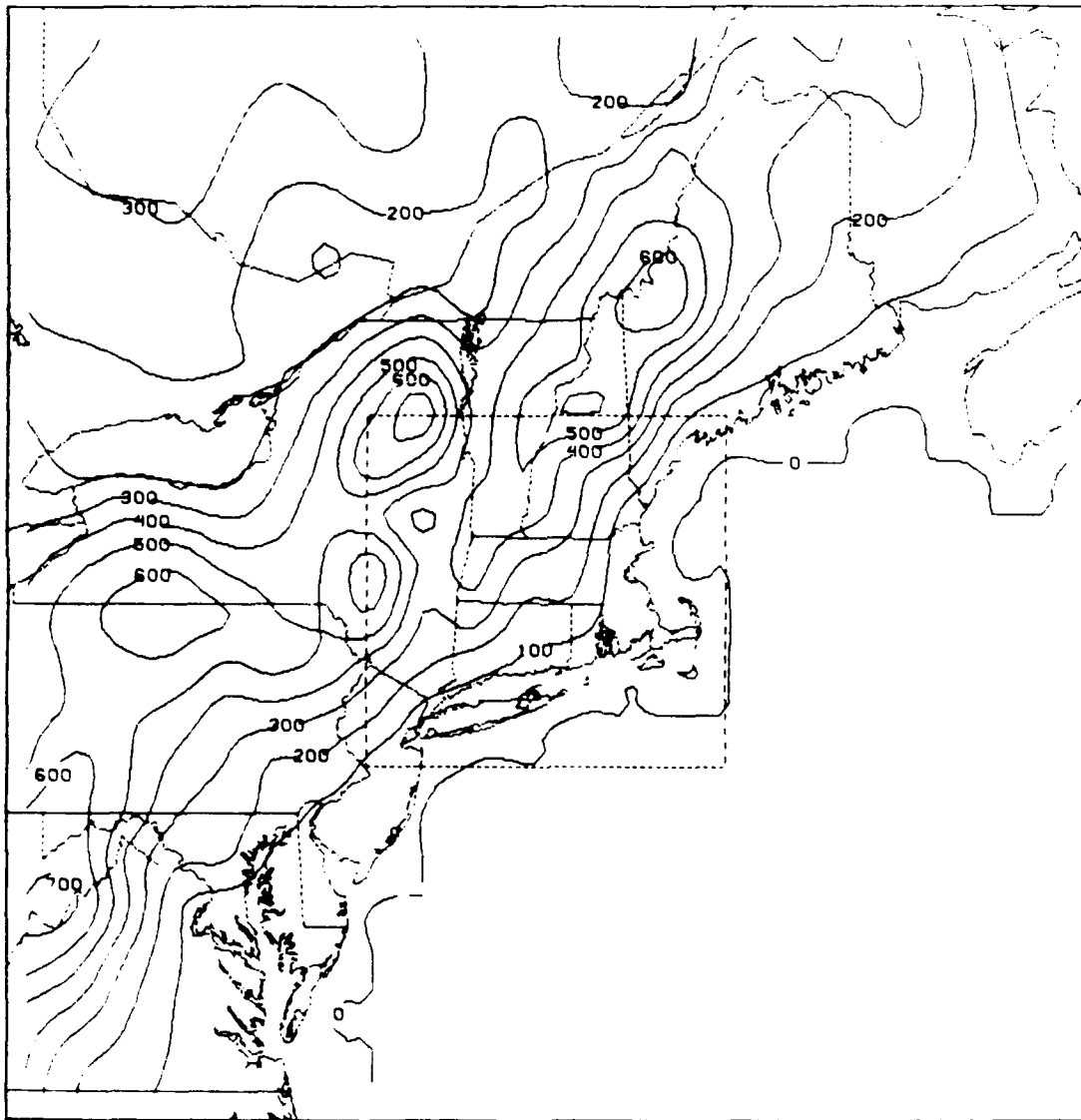
As discussed in section 3, the model's boundary-layer parameterization scheme requires a grid box to be composed entirely of either land or water, but the surface roughness parameter can be adjusted to be consistent with an average value for a grid box with a mixture of land and water. This means some of the surface roughness effects of the smaller scale features can be included in the model, even though the coastline is a "blocky" approximation to the actual coastline shown in Fig. 13 for use in the surface flux calculations. U.S. Geologic Survey maps were used to make a careful subjective estimate of the percent of water coverage for each grid box, centered on the thermodynamic grid points shown in Fig. 13. A contour plot of percent water coverage for the FGM domain that resulted from this procedure is shown in Fig. 17. Notice how well even subtle variations in the coastline are captured in the contouring, and the influence of some important inland bodies of water, such as the Hudson River, the Quabbin Reservoir, and Lake Winnepesaukee (see Fig. 16). For the boundary-layer parameterization, a grid point is considered to be water if its grid box is composed of more than 50% water coverage. The island of Nantucket presented a problem in this analysis. Review of Fig. 13 shows that Nantucket lies nearly in the middle of a square formed by four grid points. This means that its land is almost equally divided between the four grid boxes represented by those four grid points. Rather than have the model perceive a 40×40 km area of partial land coverage, the decision was made to "move" Nantucket approximately 10 km northwest so that its land mass fell entirely within one grid box. This move is obvious in Fig. 17, in which the partial land contour representing Nantucket is displaced northwestward of the geographic location of the island.

The initial smoothed, partial envelope terrain field for the CGM is shown in Fig. 18. During the first test simulations using the New England domain, it became apparent that there was an incompatibility between the CGM terrain field and the flow relaxation boundary condition used on the CGM lateral boundaries. The results of these simulations and the changes in the CGM terrain that resulted are



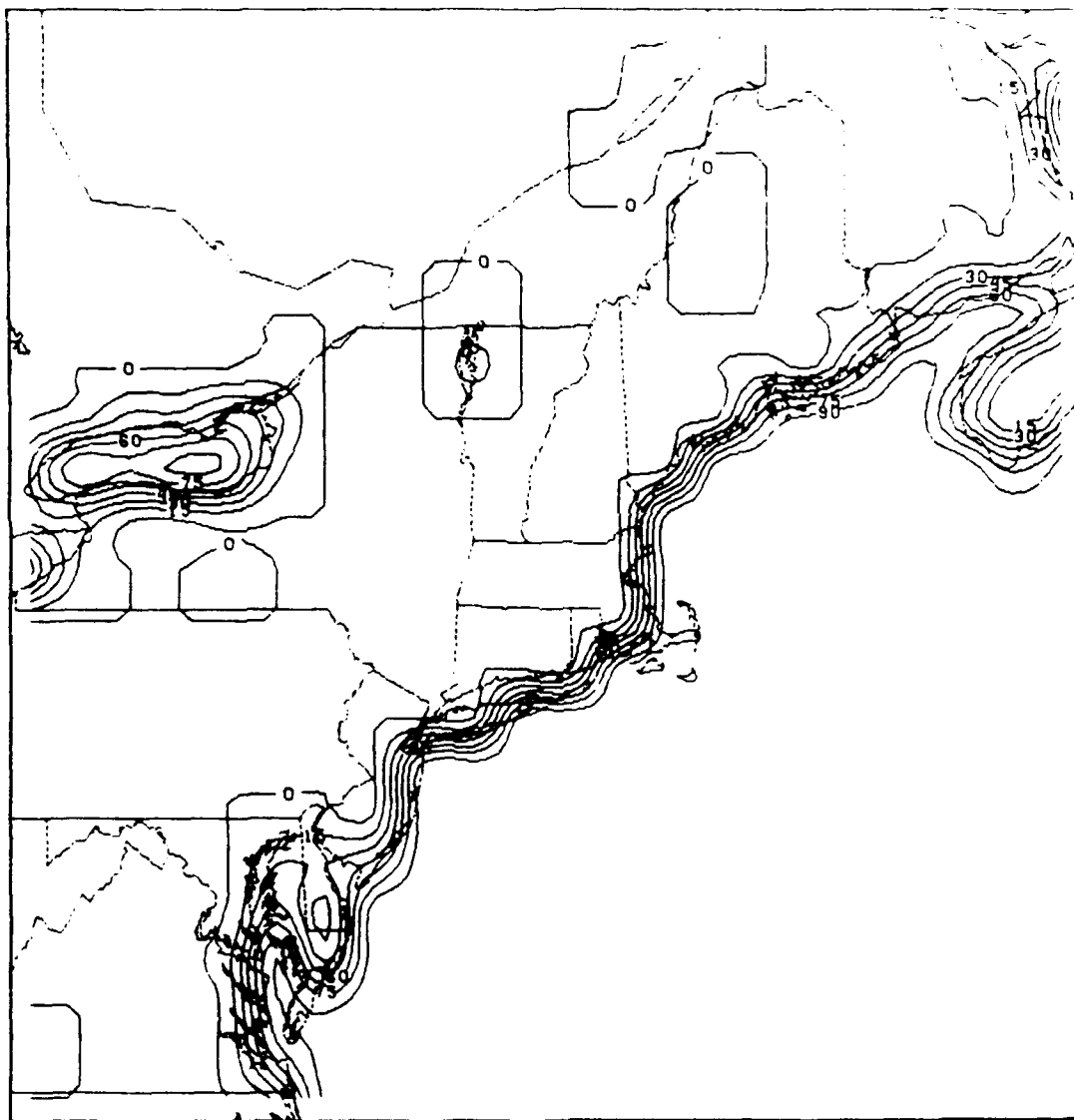
WATER COVERAGE (%)

Fig. 17. Percent water coverage in each grid box for FGM domain.



CGM SURFACE ELEVATION (M)

Fig. 18. Unmodified, smoothed, partial envelope terrain field for the CGM domain.



WATER COVERAGE (%)

Fig. 19. Percent water coverage in each grid box for CGM domain.

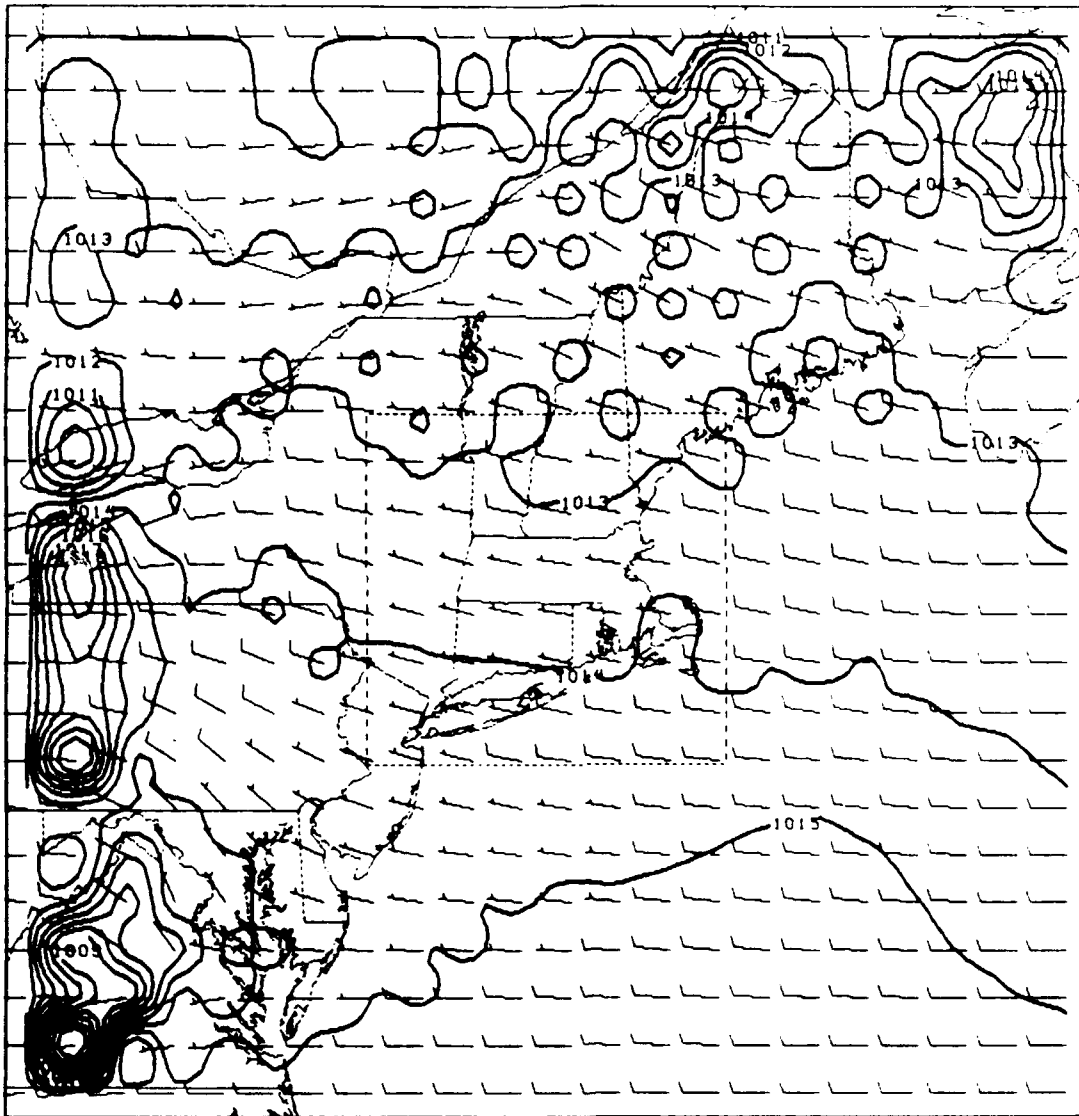
discussed in the next section. A fractional water coverage field for the CGM was constructed in a manner similar to that used for the FGM, and this field is shown in Fig. 19.

b. Initial simulations and modifications to CGM terrain field

A very simple set of initial conditions was chosen for these first test simulations of the model on realistic terrain. The thermodynamic and moisture profiles were initialized as the U.S. Standard Atmosphere temperature structure at all locations with a relative humidity of 50%. The winds were initialized as westerly at all heights with a magnitude 4 m s^{-1} , and the surface pressure field was set to be in near-geostrophic balance with these winds. The simulation was started at 0530 local time on 01 June, which is shortly after sunrise for the center of the domain. The boundary-layer height was initialized at $\sigma_h = 0.96$ over the entire domain, yielding a boundary-layer thickness of just over 300 m.

Figure 20 shows the sea level pressure and boundary layer wind fields in the CGM domain after 1 h simulated time. Comparison with Fig. 18 makes it clear that large pressure anomalies are being created at grid points near the boundary where the terrain height differs substantially from the terrain height of a boundary point. The explanation for this is really quite straightforward. The flow relaxation boundary condition employs a Newtonian damping-type term to relax the interior value of a quantity toward the value of that quantity on the nearest boundary point (Davies 1976). A weighting function controls the amount of damping in the relaxation region, smoothly decreasing the influence of the boundary point as the distance from the boundary increases over a $5\Delta x$ -wide region. Therefore, surface pressure values in the relaxation region will be forced toward the boundary value of surface pressure. If the boundary point is at a different elevation than the interior point, the forcing will tend to relax the interior point to the boundary surface pressure even though this value is not consistent in terms of sea level reduced pressure. While it may appear that this situation could be corrected using sea level pressure in the relaxation condition rather than surface pressure, similar height dependencies exist for the other variables, such as temperature and moisture, with similar negative impacts on the simulation.

Problems arising from use of the relaxation condition in complex terrain near



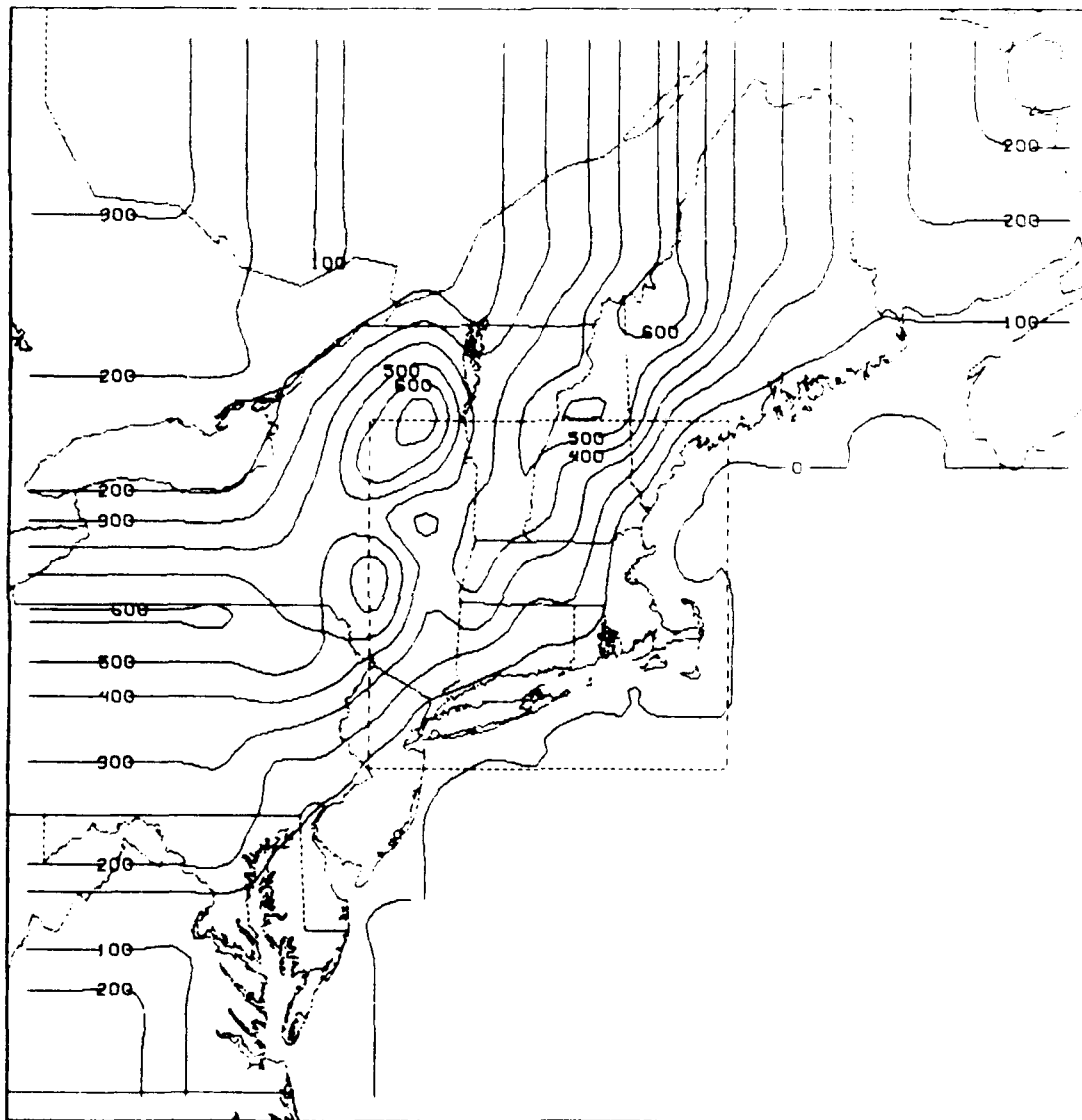
CGM VECTOR WINDS

CGM SURFACE PRESSURE (MB)

Fig. 20. Sea level pressure and boundary layer wind fields for CGM domain after 1 h simulation when the terrain field shown in Fig. 18 is used.

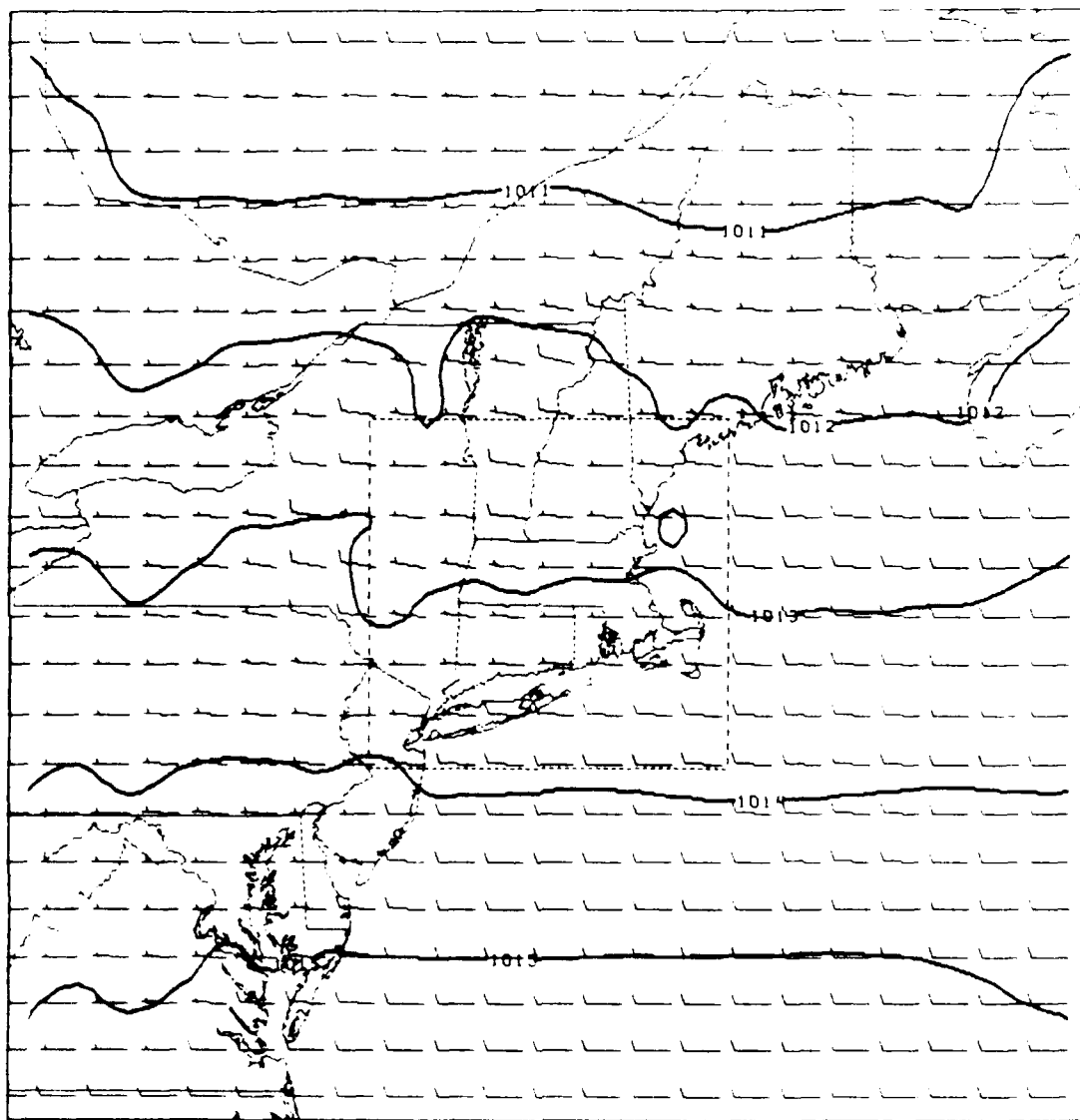
the boundary can be reduced by greatly smoothing the terrain field in the relaxation region. The only way to truly eliminate this source of accumulating error is to set the terrain height of each point in the relaxation region to be equal to the height of its nearest boundary point. To do this, the terrain heights of the innermost grid points in the relaxation region ($5\Delta x$ from the boundary) were extended outward to the boundary. This allows variation in the terrain heights along the boundary and produces the "corrugated" outer terrain field shown in Fig. 21. The fact that this modified terrain field does not match a smoothed actual terrain for the outermost region of the CGM reinforces the notion that the solution in the relaxation region should not be interpreted as a physical solution, but as a modified solution that isolates the interior from the negative impacts of the lateral boundaries. Care will need to be taken, however, in specifying the large-scale forcing on the outer CGM lateral boundaries since the terrain heights at these grid points will not necessarily match the terrain heights in the dataset supplying the external forcing. This source of error was already present, of course, since the large-scale forcing data will come from a much coarser resolution grid whose smoothed terrain field would not necessarily match that of the CGM even without the modification described above.

Figure 22 shows the sea level pressure and boundary layer wind fields after 1 h simulated time for the same initial conditions used to produce Fig. 20, but when the modified terrain field shown in Fig. 21 is used. The solution is obviously much smoother, and the large scale forcing that the CGM provides for the FGM appears much more natural. The FGM solution for this same simulation at this same time is shown in Fig. 23. Even in these early stages of the simulation, the effects of the terrain are visible in the winds and pressure patterns. The Mt. Washington area near the northern boundary of the FGM appears to be exhibiting some perturbations in pressure that may be a combination of physically realistic lee-wave phenomena and aliasing at the CGM/FGM interface. As mentioned above, some special smoothing may need to be applied to the terrain in this area because of its closeness to the edge of the FGM.



CGM SURFACE ELEVATION (M)

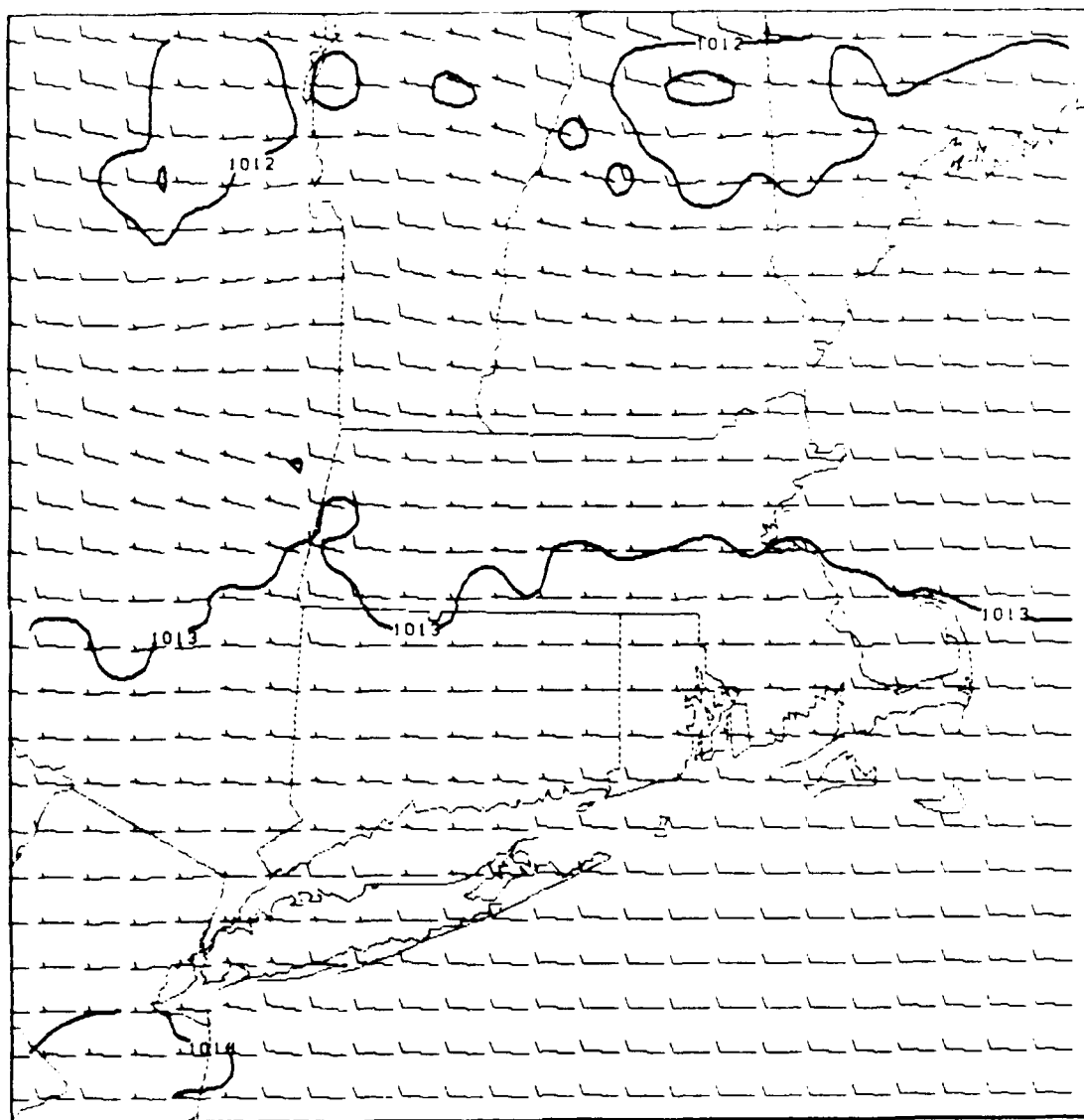
Fig. 21. Modified terrain field for the CGM domain that sets the terrain height of points in the relaxation region the same as the nearest boundary point for consistency with the relaxation boundary condition.



CGM VECTOR WINDS

CGM SURFACE PRESSURE (MB)

Fig. 22. Sea level pressure and boundary layer wind fields for CGM domain after 1 h simulation when the modified terrain field shown in Fig. 21 is used.



VECTOR WINDS

SURFACE PRESSURE (MB)

Fig. 23. Sea level pressure and boundary layer wind fields for FGM domain after 1 h simulation when the modified terrain field shown in Fig. 21 is used.

6. Conclusions and future work

This paper has presented a mesoscale model developed by transforming the equations of motion into a coordinate system in which the boundary-layer top is a coordinate surface. This leads to a means of parameterizing boundary-layer processes in a simple and computationally efficient manner while still incorporating those processes that should be important on the mesoscale. Tests with the model demonstrate that the boundary-layer coordinate system that has been developed is robust and can model the real atmosphere reasonably well, despite having a very limited vertical resolution. In addition, the boundary-layer parameterizations, though simple, forecast the gross characteristics of both stable and unstable boundary layers well.

Additional work is necessary to test this dry prototype model using the southern New England complex terrain. The ability of the model to simulate the interaction of orographic and sea-breeze type phenomena has not been fully evaluated. Several nonprecipitating case studies (both sea-breeze cases and "dry" cold-frontal passages) have been identified and will be used to test the model with real data. For these simulations, synoptic scale forcing can be included on the CGM lateral boundaries by interpolating the observed fields in both time and space. In an operational setting, synoptic scale boundary forcing would be provided by output from one of the operational synoptic scale models.

While a dry mesoscale model such as the one presented here has many operational uses, it is clear that many of the situations in which a mesoscale model could provide added forecast guidance involve production and enhancement of precipitation by local circulations and complex terrain. Work is currently underway to add moist physics to the model described here so that it can be used as a more general forecasting tool.

APPENDIX A

List of Variables

$ABS(k)$	fractional absorption of radiation by water vapor for layer k
c	volumetric heat capacity
C	dimensionless constant
c_p	specific heat of dry air at constant pressure
C_p^*	a tunable function of the Richardson number
C_d, C_f, C_t	dimensionless constants taken from Zeman (1975)
c_1, c_2	nondimensional constants
$C(\mu)$	universal function for a stable boundary layer
$C_t(\mu_t)$	universal function for an unstable boundary layer
d_1	depth of diurnal cycle ($= 10$ cm)
E_{H_2O}	effective amount of water vapor in layer k
f	Coriolis parameter
F	friction term
g	acceleration of gravity
GAB	total absorption of radiation at the ground
GLW_α	absorbed part of incident solar radiation
GLW_s	scattered part of incident solar radiation
GS	soil heat flux downward into the ground
GWB	percent bulk soil saturation (top 50 cm)
GW	percent surface soil saturation
h	height of the boundary layer
IR_d	downward flux of infra-red radiation
IR_u	upward flux of infra-red radiation

k	von Kármán's constant
K	eddy viscosity
L	Obukhov's length
LH	latent heat flux at top of the surface layer
NR	net radiation at the surface
P_r	precipitation rate
Q	heating term
q_*	$-LH/u_*$
S_0	solar constant as a function of day of year
SH	sensible heat flux at top of the surface layer
SH_h	sensible heat flux at the boundary-layer inversion
\bar{T}	average temperature of the soil, assumed to be invariant with depth (in practice, the 50 cm soil temperature is used)
TS	temperature at the top of the surface layer
T_c	critical temperature dividing the region of weak temperature dependence of τ to that of strong dependence of τ
$T_\theta(z,t)$	soil temperature at depth z and time t
u_*	friction velocity
u_{g0}, v_{g0}	components of the surface geostrophic wind
V_0	vector speed just above the boundary layer
V_0	windspeed just above the boundary layer
VSH	virtual sensible heat flux at the surface
VSH_h	virtual sensible heat flux at the boundary-layer inversion
V	vector velocity ($= u\mathbf{i} + v\mathbf{j}$)
w_*	convective velocity scale $= \left[\frac{g}{TS} VSH h \right]^{\frac{1}{3}}$
W_{max}	field capacity soil moisture
z_0	roughness length (function of location)
z_t	thickness of the next model layer above the PBL
ZT	zenith angle for time of day and location
α	specific volume
α_s	scattering albedo for the atmosphere (if clouds are present they determine the scattering albedo)

α_g	albedo of ground surface as a function of hour angle and surface characteristics (Wetzel 1978)
∇	horizontal gradient operator ($= i\partial/\partial x + j\partial/\partial y$)
γ	potential temperature lapse rate above the PBL
$\Delta\theta$	jump discontinuity at the top of the boundary layer
$\Delta\mathbf{u}$	vector difference between the wind just above the boundary layer (\mathbf{V}_0) and the wind in the boundary layer ($\Delta\mathbf{u} = \Delta u\mathbf{i} + \Delta v\mathbf{j}$)
θ_∞	potential temperature at the top of the PBL
θ_0	potential temperature at the ground
θ_i	potential temperature of the free atmosphere above the PBL
θ_p	potential temperature above jump discontinuity
θ_s	potential temperature at the top of surface layer
θ_h	potential temperature at the top of the PBL
θ_*	$-SH/u_*$
$\bar{\theta}$	mean potential temperature
η	boundary-layer coordinate in vertical direction
$\dot{\eta}$	boundary-layer coordinate vertical velocity
κ	thermal conductivity of soil
λ	latent heat of evaporation
μ	ku_*/fL
μ_1	h/L
ξ	angle between the surface stress and the geostrophic wind above the boundary layer
ρ	density of air
ρ_w	density of water (1 gm cm^{-3})
σ	Stephan-Boltzmann constant
σ_h	height of the boundary layer in σ -coordinates
τ_p	period of cycle
$\bar{\tau}, \tau$	mean total transmission functions for effective absorber u^* at temperature T
τ_{xy}	surface stress vector
ϕ	geopotential
ω	frequency of the variance of soil surface temperature
ω_{bv}	Brunt-Vaisala frequency $= \left(\frac{g\gamma}{T\bar{S}} \right)^{1/2}$

APPENDIX B

Derivation and Energy Conservation of the Eta-Coordinate System

a. Derivation of the equations in η -coordinates

The most common form of terrain following coordinate is the σ -system where

$$\sigma = \frac{(p - p_t)}{\pi} \quad (B.1)$$

where $\pi = (p_s - p_t)$, and p_s and p_t are the pressures at the surface and the top of the model domain, respectively. The equation set in this coordinate system may be written (Haltiner and Williams 1980)

$$\frac{dV}{dt} + \nabla\phi + \sigma\alpha\nabla\pi + f\mathbf{k} \times \mathbf{V} = \mathbf{F} \quad (B.2)$$

$$\frac{\partial\phi}{\partial\sigma} = -\pi\alpha \quad (B.3)$$

$$\frac{\partial\pi}{\partial t} + \nabla \cdot \pi\mathbf{V} + \pi\frac{\partial\dot{\sigma}}{\partial\sigma} = 0 \quad (B.4)$$

$$c_p \frac{dT}{dt} - \alpha\omega = Q \quad (B.5)$$

where

$$\omega = \frac{dp}{dt} = \pi\dot{\sigma} + \sigma(\partial\pi/\partial t + \mathbf{V} \cdot \nabla\pi)$$

and

$$\nabla = i\partial/\partial x + j\partial/\partial y$$

In order to preserve conservative properties in the finite difference equations, we write the total derivatives in flux form, which can be obtained with the aid of the continuity equation (B.4). Equations (B.2) and (B.5) can then be written

$$\frac{\partial\pi\mathbf{V}}{\partial t} + \frac{\partial u\pi\mathbf{V}}{\partial x} + \frac{\partial v\pi\mathbf{V}}{\partial y} + \frac{\partial\pi\mathbf{V}\dot{\sigma}}{\partial\sigma} = -\pi\nabla\phi - \pi\alpha\sigma\nabla\pi - f\mathbf{k} \times \pi\mathbf{V} + \pi\mathbf{F} \quad (B.6)$$

$$\frac{\partial \pi T}{\partial t} + \frac{\partial u \pi T}{\partial x} + \frac{\partial v \pi T}{\partial y} + \frac{\partial \pi T \sigma}{\partial \sigma} = \frac{\pi \alpha}{c_F} \omega + \frac{\pi Q}{c_F} \quad (B.7)$$

The transformation to η -coordinates is carried out formally by using the definition of η

$$\eta = \frac{\sigma - \sigma_h}{H} \quad H = \begin{cases} \sigma_h & \sigma < \sigma_h \\ 1 - \sigma_h & \sigma > \sigma_h \end{cases} \quad (B.8)$$

so that

$$\sigma = \eta H + \sigma_h \quad (B.9)$$

and for some dependent variable A

$$\left(\frac{\partial A}{\partial \sigma} \right)_\sigma = \frac{1}{H} \frac{\partial A}{\partial \eta}$$

$$\left(\frac{\partial A}{\partial s} \right)_\sigma = \left(\frac{\partial A}{\partial s} \right)_\eta - \frac{1}{H} \frac{\partial A}{\partial \eta} \left(\frac{\partial \sigma}{\partial s} \right)_\eta$$

where $s = x, y$, or t . Then the η -coordinate set equivalent to (B.6), (B.3), (B.4), and (B.7) is

$$\begin{aligned} \frac{\partial \pi H V}{\partial t} + \frac{\partial u \pi H V}{\partial x} + \frac{\partial v \pi H V}{\partial y} + \frac{\partial \pi V H \eta}{\partial \eta} = \\ - \pi H \nabla \phi - \pi H \alpha \nabla \sigma \pi - f \mathbf{k} \times \pi H V + \pi H F \end{aligned} \quad (B.10)$$

$$\frac{\partial \phi}{\partial \eta} = -\pi H \alpha \quad (B.11)$$

$$\frac{\partial \pi H}{\partial t} + \nabla \cdot \pi H V + \pi \frac{\partial H \eta}{\partial \eta} = 0 \quad (B.12)$$

$$\frac{\partial \pi H T}{\partial t} + \frac{\partial u \pi H T}{\partial x} + \frac{\partial v \pi H T}{\partial y} + \frac{\partial \pi T H \eta}{\partial \eta} = \frac{\pi H \alpha}{c_F} \omega + \frac{\pi H Q}{c_F} \quad (B.13)$$

where now

$$\omega = \frac{dp}{dt} = \pi H \dot{\eta} + \partial(\sigma \pi) / \partial t + \mathbf{V} \cdot \nabla \sigma \pi \quad (B.14)$$

Note that σ is now a dependent variable which is a function of x, y, η and t , and is

given by (B.9). As can be seen by comparing (B.10)–(B.13) with (B.6), (B.3), (B.4), and (B.7), the transformation leads to the prognostic variables being weighted by πH in the η system instead of the π -weighting present in the σ system. Note also that terms that had been σ times derivatives of π become derivatives of the quantity $(\sigma\pi)$ in the η system.

b. Energy conservation in the η -system

In order to determine the correct finite differencing form that will preserve energy conservation in the finite difference equations, the energy conservation constraints of the continuous equations must first be derived. The analysis presented here closely follows that carried out by Haltiner and Williams (1980) for the σ -coordinate equations.

We begin with the η -coordinate momentum equation [equivalent to (B.2)]

$$\frac{d\mathbf{V}}{dt} + \nabla\phi + \alpha\nabla\sigma\pi + f\mathbf{k} \times \mathbf{V} = \mathbf{F} \quad (\text{B.15})$$

This is dotted with $\pi H \mathbf{V}$, and rewritten in the flux form with the aid of the continuity equation (B.12), to yield

$$\begin{aligned} \frac{\partial}{\partial t}(\frac{1}{2}\pi H V^2) + \nabla \cdot (\frac{1}{2}\pi H \mathbf{V} V^2) + \frac{\partial}{\partial \eta}(\frac{1}{2}\pi H \dot{\eta} V^2) = \\ -\pi H \mathbf{V} \cdot (\pi H \nabla\phi + \alpha\nabla\sigma\pi) + \pi H \mathbf{V} \cdot \mathbf{F} \end{aligned} \quad (\text{B.16})$$

The first term on the right hand side represents the kinetic energy production by the pressure force. We expand this term as follows

$$-\pi H \mathbf{V} \cdot (\nabla\phi + \alpha\nabla\sigma\pi) = -\nabla \cdot (\pi H \mathbf{V} \phi) + \phi \nabla \cdot (\pi H \mathbf{V}) - \alpha \pi H \mathbf{V} \cdot \nabla\sigma\pi$$

The continuity equation (B.12) allows this to be rewritten

$$\begin{aligned} &= -\nabla \cdot (\pi H \mathbf{V} \phi) - \phi \left(\frac{\partial \pi H}{\partial t} + \pi \frac{\partial H \dot{\eta}}{\partial \eta} \right) - \alpha \pi H \mathbf{V} \cdot \nabla\sigma\pi \\ &= -\nabla \cdot (\pi H \mathbf{V} \phi) - \phi \frac{\partial \pi H}{\partial t} - \frac{\partial \phi \pi H \dot{\eta}}{\partial \eta} + \pi H \dot{\eta} \frac{\partial \phi}{\partial \eta} - \alpha \pi H \mathbf{V} \cdot \nabla\sigma\pi \end{aligned}$$

Use of the hydrostatic equation (B.11) leads to

$$= -\nabla \cdot (\pi H \mathbf{V} \phi) - \phi \frac{\partial \pi H}{\partial t} - \frac{\partial \phi \pi H \dot{\eta}}{\partial \eta} + \pi H \dot{\eta} (-H \pi \alpha) - \alpha \pi H \mathbf{V} \cdot \nabla \sigma \pi$$

Adding and subtracting $\pi H \alpha (\partial \sigma \pi / \partial t)$, and rearranging yields

$$\begin{aligned} -\pi H \mathbf{V} \cdot (\nabla \phi + \alpha \nabla \sigma \pi) &= -\nabla \cdot (\pi H \mathbf{V} \phi) - \phi \frac{\partial \pi H}{\partial t} - \frac{\partial \phi \pi H \dot{\eta}}{\partial \eta} + \pi H \alpha \frac{\partial \sigma \pi}{\partial t} \\ &\quad - H \pi \alpha \left(\frac{\partial \sigma \pi}{\partial t} + \mathbf{V} \cdot \nabla \sigma \pi + \pi H \dot{\eta} \right) \end{aligned}$$

Then using the definition of ω , (B.14), and expanding the time derivatives of the products leads to

$$\begin{aligned} &= -\nabla \cdot (\pi H \mathbf{V} \phi) - \frac{\partial \phi \pi H \dot{\eta}}{\partial \eta} - (H \phi - H \pi \alpha \sigma) \frac{\partial \pi}{\partial t} - \phi \pi \frac{\partial H}{\partial t} + \pi^2 H \alpha \frac{\partial \sigma}{\partial t} \\ &\quad - \pi H \alpha \omega \end{aligned}$$

Now, (B.11) can be rewritten as $\partial(\phi \sigma) / \partial \eta = -H(\pi \sigma \alpha - \phi)$, and this along with use of (B.11) directly leads to

$$= -\nabla \cdot (\pi H \mathbf{V} \phi) - \frac{\partial \phi \pi H \dot{\eta}}{\partial \eta} - \frac{\partial \phi \sigma}{\partial \eta} \frac{\partial \pi}{\partial t} - \phi \pi \frac{\partial H}{\partial t} - \pi \frac{\partial \phi}{\partial \eta} \frac{\partial \sigma}{\partial t} - \pi H \alpha \omega$$

Noting that π is not a function of η and that $\partial(\partial \sigma / \partial t) / \partial \eta = \partial H / \partial t$ leads to the result that

$$\begin{aligned} -\pi H \mathbf{V} \cdot (\nabla \phi + \alpha \nabla \sigma \pi) &= -\nabla \cdot (\pi H \mathbf{V} \phi) - \frac{\partial}{\partial \eta} \left(\phi \pi H \dot{\eta} + \phi \sigma \frac{\partial \pi}{\partial t} \right) \\ &\quad - \frac{\partial}{\partial \eta} \left(\phi \pi \frac{\partial \sigma}{\partial t} \right) - \pi H \alpha \omega \end{aligned} \tag{B.17}$$

We form the total energy equation by using (B.16) with the substitution given by (B.17), and adding it to the thermodynamic equation (B.13) which can be written in the form

$$\frac{\partial}{\partial t} (\pi H c_p T) + \nabla \cdot (\pi H \mathbf{V} c_p T) + \frac{\partial}{\partial \eta} (\pi H c_p T H \dot{\eta}) = \pi H (\alpha \omega + Q) \tag{B.18}$$

to yield

$$\begin{aligned}
& \frac{\partial}{\partial t} \left(\frac{1}{2} \pi H V^2 + \pi H c_p T \right) + \nabla \cdot \mathbf{V} \left(\frac{1}{2} \pi H V^2 + \pi H c_p T + \pi H \phi \right) \\
& + \frac{\partial}{\partial \eta} \left(\frac{1}{2} \pi V^2 H \dot{\eta} + \pi c_p T H \dot{\eta} + \pi \phi H \dot{\eta} \right) + \frac{\partial}{\partial \eta} \left(\phi \sigma \frac{\partial \pi}{\partial t} \right) + \frac{\partial}{\partial \eta} \left(\phi \pi \frac{\partial \sigma}{\partial t} \right) \\
& = \pi H (Q + \mathbf{V} \cdot \mathbf{F})
\end{aligned} \tag{B.19}$$

If (B.19) is integrated from $\eta = -1$ (where $\sigma = 0$) to $\eta = 1$ (where $\sigma = 1$), we obtain

$$\begin{aligned}
& \frac{\partial}{\partial t} \left[\phi_s p_s + \int_{-1}^1 \pi H \left(\frac{1}{2} V^2 + c_p T \right) d\eta \right] + \nabla \cdot \int_{-1}^1 \pi H \mathbf{V} \left(\frac{1}{2} V^2 + c_p T + \phi \right) d\eta \\
& = \int_{-1}^1 \pi H (Q + \mathbf{V} \cdot \mathbf{F}) d\eta
\end{aligned} \tag{B.20}$$

where we have used $H \dot{\eta} = 0$ at $\eta = -1$ and 1 , $\partial \sigma / \partial t = 0$ at $\eta = -1$ and 1 , and $\phi (\partial \pi / \partial t) = \partial (\phi_s p_s) / \partial t$. This is precisely the same energy relation derived by Haltiner and Williams [1980, their Eq. (7-42)] for the σ -coordinate equations, if we note that $H d\eta = d\sigma$. It is desirable for this energy constraint on the continuous equations to also hold for the finite difference equations. As will be seen, this will determine the appropriate form for the finite difference equation set, and for the method of vertical finite differencing.

c. The energy-conserving finite difference equations

The finite difference form of (B.10) is

$$\begin{aligned}
& \frac{\partial}{\partial t} (\pi H \mathbf{V}_k) + \frac{\partial}{\partial x} (u_k \pi H \mathbf{V}_k) + \frac{\partial}{\partial y} (v_k \pi H \mathbf{V}_k) + \\
& \frac{\pi}{\Delta \eta} \left[(H \dot{\eta})_{k+1/2} \hat{\mathbf{V}}_{k+1/2} - (H \dot{\eta})_{k-1/2} \hat{\mathbf{V}}_{k-1/2} \right] = \\
& - \pi H [\nabla \phi_k + \alpha_k \nabla \sigma_k \pi] - f \mathbf{k} \times \pi H \mathbf{V}_k + \pi H \mathbf{F}_k
\end{aligned} \tag{B.21}$$

where H takes on the appropriate value as given by (B.8) depending on whether the

layer k is above or below σ_k . The indices $(k-1/2)$ and $(k+1/2)$ refer to the layer interfaces bounding layer k above and below, respectively. The quantity \hat{V} is the interpolation of V from adjacent layers to the interface. Haltiner and Williams (1980) show that the advective terms will conserve both V and $(V \cdot V)/2$ if

$$\hat{V}_{k+1/2} = \frac{1}{2}(V_{k+1} + V_k) \quad (B.22)$$

We wish to insure energy conservation of the rhs as well. The Coriolis terms do not contribute, and we will ignore the friction term and concentrate on the pressure gradient term. As with the continuous equations, we find the rate of working by the pressure gradient terms by taking $V_k \cdot$ of the first term on the rhs of (B.21) to obtain

$$\begin{aligned} -\pi H V_k \cdot [\nabla \phi_k + \alpha_k \nabla \sigma_k \pi] &= -\nabla \cdot (\pi H V_k \phi_k) + \phi_k \nabla \cdot (\pi H V_k) \\ &\quad - \alpha_k \pi H V_k \cdot \nabla \sigma_k \pi \end{aligned} \quad (B.23)$$

The finite difference form of the continuity equation is

$$\frac{\partial \pi H}{\partial t} + \nabla \cdot \pi H V_k + \frac{\pi}{\Delta \eta} [(H\dot{\eta})_{k+1/2} - (H\dot{\eta})_{k-1/2}] = 0 \quad (B.24)$$

so, (B.23) can be rewritten

$$\begin{aligned} -\pi H V_k \cdot [\nabla \phi_k + \alpha_k \nabla \sigma_k \pi] &= -\nabla \cdot (\pi H V_k \phi_k) \\ &\quad - \phi_k \left\{ \frac{\partial \pi H}{\partial t} + \frac{\pi}{\Delta \eta} [(H\dot{\eta})_{k+1/2} - (H\dot{\eta})_{k-1/2}] \right\} - \alpha_k \pi H V_k \cdot \nabla \sigma_k \pi \end{aligned}$$

Adding and subtracting $\frac{\pi}{\Delta \eta} [(H\dot{\eta})_{k+1/2} \hat{\phi}_{k+1/2} - (H\dot{\eta})_{k-1/2} \hat{\phi}_{k-1/2}]$ yields

$$\begin{aligned} &= -\nabla \cdot (\pi H V_k \phi_k) - \phi_k \frac{\partial \pi H}{\partial t} - \frac{\pi}{\Delta \eta} [(H\dot{\eta})_{k+1/2} \hat{\phi}_{k+1/2} - (H\dot{\eta})_{k-1/2} \hat{\phi}_{k-1/2}] \\ &\quad + \frac{\pi}{\Delta \eta} [(H\dot{\eta})_{k+1/2} (\hat{\phi}_{k+1/2} - \phi_k) - (H\dot{\eta})_{k-1/2} (\hat{\phi}_{k-1/2} - \phi_k)] \\ &\quad - \alpha_k \pi H V_k \cdot \nabla \sigma_k \pi \end{aligned}$$

Now, adding and subtracting $H\pi\alpha_k(\partial\sigma_k\pi/\partial t)$ leads to

$$\begin{aligned}
-\pi H \mathbf{V}_k \cdot [\nabla \phi_k + \alpha_k \nabla \sigma_k \pi] &= -\nabla \cdot (\pi H \mathbf{V}_k \phi_k) \\
&- \frac{\pi}{\Delta \eta} [(H\dot{\eta})_{k+1/2} \hat{\phi}_{k+1/2} - (H\dot{\eta})_{k-1/2} \hat{\phi}_{k-1/2}] \\
&- (\phi_k H - H\pi\alpha_k \sigma_k) \frac{\partial \pi}{\partial t} - \phi_k \pi \frac{\partial H}{\partial t} + H\pi^2 \alpha_k \frac{\partial \sigma_k}{\partial t} \\
&- \alpha_k \pi H \left[\frac{\partial \sigma_k \pi}{\partial t} + \mathbf{V}_k \cdot \nabla \sigma_k \pi \right] \\
&+ \frac{\pi}{\Delta \eta} [(H\dot{\eta})_{k+1/2} (\hat{\phi}_{k+1/2} - \phi_k) - (H\dot{\eta})_{k-1/2} (\hat{\phi}_{k-1/2} - \phi_k)]
\end{aligned} \tag{B.25}$$

Now, it is easy to verify that

$$\frac{\partial \sigma_k}{\partial t} = \frac{\sigma_k}{H} \frac{\partial H}{\partial t} \tag{B.26}$$

So, (B.25) can be written

$$\begin{aligned}
-\pi H \mathbf{V}_k \cdot [\nabla \phi_k + \alpha_k \nabla \sigma_k \pi] &= -\nabla \cdot (\pi H \mathbf{V}_k \phi_k) \\
&- \frac{\pi}{\Delta \eta} [(H\dot{\eta})_{k+1/2} \hat{\phi}_{k+1/2} - (H\dot{\eta})_{k-1/2} \hat{\phi}_{k-1/2}] \\
&- [\phi_k H - H\pi\alpha_k \sigma_k] \frac{\partial \pi}{\partial t} - \frac{\pi}{H} [\phi_k H - H\pi\alpha_k \sigma_k] \frac{\partial H}{\partial t} \\
&- \alpha_k \pi H \left[\frac{\partial \sigma_k \pi}{\partial t} + \mathbf{V}_k \cdot \nabla \sigma_k \pi \right] \\
&+ \frac{\pi}{\Delta \eta} [(H\dot{\eta})_{k+1/2} (\hat{\phi}_{k+1/2} - \phi_k) - (H\dot{\eta})_{k-1/2} (\hat{\phi}_{k-1/2} - \phi_k)]
\end{aligned} \tag{B.27}$$

But, using the finite difference form of $\partial(\phi\sigma)/\partial\eta = -H(\pi\sigma\alpha - \phi)$, and noting that $\partial\pi/\partial t$ and $\partial H/\partial t$ are not functions of η , we can write

$$\begin{aligned}
-\pi H \mathbf{V}_k \cdot [\nabla \phi_k + \alpha_k \nabla \sigma_k \pi] &= -\nabla \cdot (\pi H \mathbf{V}_k \phi_k) \\
&- \frac{\pi}{\Delta \eta} [(H\dot{\eta})_{k+1/2} \hat{\phi}_{k+1/2} - (H\dot{\eta})_{k-1/2} \hat{\phi}_{k-1/2}] \\
&- \frac{1}{\Delta \eta} \left[\hat{\sigma}_{k+1/2} \hat{\phi}_{k+1/2} \frac{\partial \pi}{\partial t} - \hat{\sigma}_{k-1/2} \hat{\phi}_{k-1/2} \frac{\partial \pi}{\partial t} \right] \\
&- \frac{1}{\Delta \eta} \left[\hat{\phi}_{k+1/2} \pi \frac{\hat{\sigma}_{k+1/2} \partial H}{H \partial t} - \hat{\phi}_{k-1/2} \pi \frac{\hat{\sigma}_{k-1/2} \partial H}{H \partial t} \right] \\
&- \alpha_k \pi H \left[\frac{\partial \sigma_k \pi}{\partial t} + \mathbf{V}_k \cdot \nabla \sigma_k \pi \right] \\
&+ \frac{\pi}{\Delta \eta} [(H\dot{\eta})_{k+1/2} (\hat{\phi}_{k+1/2} - \phi_k) - (H\dot{\eta})_{k-1/2} (\hat{\phi}_{k-1/2} - \phi_k)]
\end{aligned} \tag{B.28}$$

Using (B.26) again leads to our final result

$$\begin{aligned}
-\pi H \mathbf{V}_k \cdot [\nabla \phi_k - \alpha_k \nabla \sigma_k \pi] &= -\nabla \cdot (\pi H \mathbf{V}_k \phi_k) \\
&- \frac{\pi}{\Delta \eta} [(H\dot{\eta})_{k+1/2} \hat{\phi}_{k+1/2} - (H\dot{\eta})_{k-1/2} \hat{\phi}_{k-1/2}] \\
&- \frac{1}{\Delta \eta} \left[\hat{\sigma}_{k+1/2} \hat{\phi}_{k+1/2} \frac{\partial \pi}{\partial t} - \hat{\sigma}_{k-1/2} \hat{\phi}_{k-1/2} \frac{\partial \pi}{\partial t} \right] \\
&- \frac{1}{\Delta \eta} \left[\hat{\phi}_{k+1/2} \pi \frac{\partial \hat{\sigma}_{k+1/2}}{\partial t} - \hat{\phi}_{k-1/2} \pi \frac{\partial \hat{\sigma}_{k-1/2}}{\partial t} \right] \\
&- \alpha_k \pi H \left[\frac{\partial \sigma_k \pi}{\partial t} + \mathbf{V}_k \cdot \nabla \sigma_k \pi \right] \\
&+ \frac{\pi}{\Delta \eta} [(H\dot{\eta})_{k+1/2} (\hat{\phi}_{k+1/2} - \phi_k) - (H\dot{\eta})_{k-1/2} (\hat{\phi}_{k-1/2} - \phi_k)]
\end{aligned} \tag{B.29}$$

On term by term comparison with (B.17), it is clear that (B.29) will match the continuous equations, and conserve energy in the same way on summation over all layers, if we specify that ω is defined by

$$\begin{aligned}
\pi H \alpha_k \omega_k &= \alpha_k \pi H \left[\frac{\partial \sigma_k \pi}{\partial t} + \mathbf{V}_k \cdot \nabla \sigma_k \pi \right] \\
&+ \frac{\pi}{\Delta \eta} [(H\dot{\eta})_{k+1/2} (\hat{\phi}_{k+1/2} - \phi_k) - (H\dot{\eta})_{k-1/2} (\hat{\phi}_{k-1/2} - \phi_k)]
\end{aligned} \tag{B.30}$$

This definition of ω is precisely what is needed to specify the finite difference form of the thermodynamic and hydrostatic equations, which we will derive next.

In order to show the constraints placed on the finite difference form of the thermodynamic equation, we need to first show two alternative finite difference forms of the total derivative. For a variable A at level k , we can write the total derivative in "flux form" as

$$\begin{aligned} \pi H \frac{dA_k}{dt} &= \frac{\partial \pi H A_k}{\partial t} + \mathbf{V}_k \cdot \nabla \pi H A_k \\ &+ \frac{\pi}{\Delta \eta} \left[(H\dot{\eta})_{k+1/2} \hat{A}_{k+1/2} - (H\dot{\eta})_{k-1/2} \hat{A}_{k-1/2} \right] \end{aligned} \quad (\text{B.31})$$

But use of the continuity equation (B.24) allows this to be rewritten in an "advective form" consistent with the flux form as

$$\begin{aligned} \pi H \frac{dA_k}{dt} &= \pi H \left[\frac{\partial A_k}{\partial t} + \mathbf{V}_k \cdot \nabla A_k \right] + \\ &\frac{\pi}{\Delta \eta} \left[(H\dot{\eta})_{k+1/2} (\hat{A}_{k+1/2} - A_k) - (H\dot{\eta})_{k-1/2} (\hat{A}_{k-1/2} - A_k) \right] \end{aligned} \quad (\text{B.32})$$

For frictionless, adiabatic motion, the potential temperature is conserved, so $d\theta/dt = 0$. The finite difference version of this in flux form is

$$\frac{\partial \pi H \theta_k}{\partial t} + \nabla \cdot \pi H \mathbf{V}_k \theta_k + \frac{\pi}{\Delta \eta} \left[(H\dot{\eta})_{k+1/2} \hat{\theta}_{k+1/2} - (H\dot{\eta})_{k-1/2} \hat{\theta}_{k-1/2} \right] = 0 \quad (\text{B.33})$$

In order to have θ and θ^2 conserved (Haltiner and Williams, 1980), we define

$$\hat{\theta}_{k+1/2} = \frac{1}{2}(\theta_k + \theta_{k+1}) \quad (\text{B.34})$$

We take the potential temperature to be defined by

$$\theta_k \equiv T_k / P_k \quad (\text{B.35})$$

and

$$P_k = \left[\frac{1}{2}(p_{k-1/2} + p_{k+1/2}) / 1000 \right]^\kappa \quad (\text{B.36})$$

The conservation of θ can be written in advective form, (B.32), as

$$\pi H \left[\frac{\partial \theta_k}{\partial t} + \mathbf{V}_k \cdot \nabla \theta_k \right] + \frac{\pi}{\Delta \eta} \left[(H\dot{\eta})_{k+1/2} (\hat{\theta}_{k+1/2} - \theta_k) + (H\dot{\eta})_{k-1/2} (\theta_k - \hat{\theta}_{k-1/2}) \right] = 0$$

Substituting the definition of θ_k , (B.35), this may be rewritten

$$\pi H \left[\frac{\partial}{\partial t} + \mathbf{V}_k \cdot \nabla \right] T_k + \pi H \frac{T_k}{P_k} \frac{\partial P_k}{\partial \sigma_k \pi} \left[\frac{\partial}{\partial t} + \mathbf{V}_k \cdot \nabla \right] \sigma_k \pi \quad (\text{B.37})$$

$$\frac{\pi}{\Delta \eta} \left[(H\dot{\eta})_{k+1/2} (P_k \hat{\theta}_{k+1/2} - T_k) + (H\dot{\eta})_{k-1/2} (T_k - P_k \hat{\theta}_{k-1/2}) \right] = 0$$

where we have made use of the fact that P_k can be considered a function of σ and π . We now add T_k times the continuity equation, (B.24), so that the first term can be rewritten in flux form, add the finite difference form of $\pi \partial T / \partial \eta$ to both sides, and multiply the whole equation by c_p to obtain

$$\begin{aligned} & \frac{\partial}{\partial t} (c_p \pi H T_k) + \nabla \cdot (c_p \pi H T_k \mathbf{V}_k) + \frac{c_p \pi}{\Delta \eta} \left[(H\dot{\eta})_{k+1/2} \hat{T}_{k+1/2} + (H\dot{\eta})_{k-1/2} \hat{T}_{k-1/2} \right] \\ & = \pi H \frac{c_p T_k}{P_k} \frac{\partial P_k}{\partial \sigma_k \pi} \left[\frac{\partial}{\partial t} + \mathbf{V}_k \cdot \nabla \right] \sigma_k \pi \quad (\text{B.38}) \\ & + \frac{c_p \pi}{\Delta \eta} \left[(H\dot{\eta})_{k+1/2} (\hat{T}_{k+1/2} - P_k \hat{\theta}_{k+1/2}) + (H\dot{\eta})_{k-1/2} (P_k \hat{\theta}_{k-1/2} - \hat{T}_{k-1/2}) \right] \end{aligned}$$

The lhs of (B.38) is the finite difference form of the lhs of (B.18), and therefore, the rhs should be equal to $\pi H \alpha \omega$ (since we are assuming $Q = 0$ here). Comparison with (B.37) shows that the first terms will be equal if

$$\alpha_k = \frac{c_p T_k}{P_k} \frac{\partial P_k}{\partial \sigma_k \pi} \quad (\text{B.39})$$

Equating the other terms leads to the following relations

$$\begin{aligned} c_p (\hat{T}_{k+1} - P_k \hat{\theta}_{k+1}) &= \phi_k - \hat{\phi}_{k+1} \\ c_p (P_k \hat{\theta}_{k-1} - \hat{T}_{k-1}) &= \hat{\phi}_{k-1} - \phi_k \end{aligned} \quad (\text{B.40})$$

When (B.35) is used in these, they can be rewritten

$$\begin{aligned}(c_p \hat{T}_{k+1/2} + \hat{\phi}_{k+1/2}) - (c_p T_k + \phi_k) &= P_k c_p (\hat{\theta}_{k+1/2} - \theta_k) \\ (c_p T_k + \phi_k) - (c_p \hat{T}_{k-1/2} + \hat{\phi}_{k-1/2}) &= P_k c_p (\theta_k - \hat{\theta}_{k+1/2})\end{aligned}\tag{B.41}$$

We can replace k by $k+1$ in the second of (B.41), add it to the first, and again use (B.35) to obtain

$$\phi_{k+1} - \phi_k = -c_p (P_{k+1} - P_k) \hat{\theta}_{k+1/2}\tag{B.42}$$

This represents a finite difference form of the hydrostatic equation that is consistent with the other equations, and provides a means of calculating the geopotentials at all layers once the geopotential is known at the lowest layer (where $k = k_{bm}$). Haltiner and Williams (1980) show that it is possible to derive an integral constraint from the energy conservation which yields the geopotential of the lowest layer in terms of the geopotential differences of all the other layers. It is pointed out, however, that this accumulates the errors of the layer calculations and leads to large errors in the geopotential of the lowest layer. Experimentation with the model verified this result. We choose a simpler method of obtaining the lowest layer geopotential which, though not strictly consistent with energy conservation, yields accurate values. Since the boundary layer parameterization provides an "surface" temperature, we use this temperature to form a "half-layer" average potential temperature

$$\hat{\theta}_{k_{bm}+1/4} = \frac{1}{2}(\theta_{k_{bm}} + \theta_{surf})$$

Then an equation of the form of (B.42) can be used to find $\phi_{k_{bm}}$ in terms of the geopotential at the surface.

The thermodynamic equation can now be written in the form used in the model by noting that (B.38) reduces to

$$\begin{aligned}\frac{\partial \pi H T_k}{\partial t} + \nabla \cdot \pi H \mathbf{V}_k T_k + \frac{\pi}{\Delta \eta} [(H \dot{\eta})_{k+1/2} P_k \hat{\theta}_{k+1/2} - (H \dot{\eta})_{k-1/2} P_k \hat{\theta}_{k-1/2}] \\ = \frac{\pi H \alpha_k}{c_p} \left[\frac{\partial}{\partial t} + \mathbf{V}_k \cdot \nabla \right] \sigma_k \pi + \frac{\pi}{c_p} Q_k\end{aligned}\tag{B.43}$$

(where we have added the diabatic heating term). Thus, the equations (B.21), (B.42), and (B.43) form a consistent finite difference set for momentum, geopotential, and temperature which conserve total energy in the same manner as the continuous equations.

d. *The complete finite difference equation set*

We restate here the finite difference equations derived above and add those not yet discussed to form the complete set used in the model. The only advective quantity in the model whose finite difference form is not discussed above is the one that governs specific humidity, q . In the absence of condensation or evaporation, however, specific humidity represents a conserved quantity that satisfies $dq/dt = 0$. We write this total derivative in the flux form given by (B.31).

The complete set of finite difference equations for momentum, ϕ , T , and q is then

$$\begin{aligned} \frac{\partial}{\partial t}(\pi H \mathbf{V}_k) + \frac{\partial}{\partial x}(u_k \pi H \mathbf{V}_k) + \frac{\partial}{\partial y}(v_k \pi H \mathbf{V}_k) + \\ \frac{\pi}{\Delta \eta} [(H\dot{\eta})_{k+1/2} \hat{\mathbf{V}}_{k+1/2} - (H\dot{\eta})_{k-1/2} \hat{\mathbf{V}}_{k-1/2}] = \\ - \pi H [\nabla \phi_k + \alpha_k \nabla \sigma_k \pi] - f \mathbf{k} \times \pi H \mathbf{V}_k + \pi H F_k \end{aligned} \quad (\text{B.21})$$

$$\phi_{k+1} - \phi_k = -c_F (P_{k+1} - P_k) \hat{\theta}_{k+1/2} \quad (\text{B.42})$$

$$\begin{aligned} \frac{\partial \pi H T_k}{\partial t} + \nabla \cdot \pi H \mathbf{V}_k T_k + \frac{\pi}{\Delta \eta} [(H\dot{\eta})_{k+1/2} P_k \hat{\theta}_{k+1/2} - (H\dot{\eta})_{k-1/2} P_k \hat{\theta}_{k-1/2}] \\ = \frac{\pi H \alpha_k}{c_P} \left[\frac{\partial}{\partial t} + \mathbf{V}_k \cdot \nabla \right] \sigma_k \pi + \frac{\pi}{c_P} Q_k + \pi H F_k \end{aligned} \quad (\text{B.43'})$$

and

$$\frac{\partial \pi H q_k}{\partial t} + \nabla \cdot \pi H \mathbf{V}_k q_k + \frac{\pi}{\Delta \eta} [(H\dot{\eta})_{k+1/2} \hat{q}_{k+1/2} - (H\dot{\eta})_{k-1/2} \hat{q}_{k-1/2}] = F_k \quad (\text{B.44})$$

where

$$\theta_k \equiv T_k / P_k \quad (\text{B.35})$$

and

$$P_k = \left[\frac{1}{2}(p_{k-1/2} + p_{k+1/2}) / 1000 \right]^\kappa \quad (\text{B.36})$$

Note that an eddy diffusion term, F_k , is added to the rhs of (B.43') and (B.44) as described in section 2 to help control noise. The finite difference form of (2.7), which calculates the rate of change of π is written

$$\frac{\partial \pi}{\partial t} = - \sum_{k=1}^{k_{bm}} \left[\frac{\partial}{\partial x} (H \pi u_k) + \frac{\partial}{\partial y} (H \pi v_k) \right] \quad (\text{B.45})$$

where H takes on the correct values above and below the boundary layer top as given by (B.8). Similarly, the finite difference form of (2.8) allows calculation of $(H\dot{\eta})$ at each interface as

$$\begin{aligned} (H\dot{\eta})_{k+1/2} = & -(\eta_{k+1/2} + 1) \left[\pi \frac{\partial \sigma_h}{\partial t} + \frac{H}{\pi} \frac{\partial \pi}{\partial t} \right] \\ & - \sum_{k=1}^k \left[\frac{\partial}{\partial x} (H \pi u_k) + \frac{\partial}{\partial y} (H \pi v_k) \right] \end{aligned} \quad (\text{B.46})$$

which can be applied after (B.45) has been solved to provide $\partial \pi / \partial t$ and after the boundary layer parameterization has provided $\partial h / \partial t$ which can be converted to $\partial \sigma_h / \partial t$. The above finite difference equations are applied on the staggered grid using the averaging and differencing schemes presented by Anthes and Warner (1978).

APPENDIX C

Creation of Terrain Fields

a. Creation of unmodified and envelope terrain

This appendix describes the procedure followed in developing the terrain fields used for the simulations discussed in section 4. A terrain field is simply an array that has an elevation value for each grid point, but unless care is taken in specifying these elevation values, the terrain field can generate spurious noise in the model—either because of an amplifying resonance-type response at $2\Delta x$ wavelengths or because of inconsistencies between the CGM and FGM terrain fields in the region of overlap between the two meshes.

As an initial step in creating the terrain field used here, elevations were read off U.S. Geologic Survey topographic maps at the latitude/longitude locations of the FGM and CGM grid points. In addition, with each grid point treated as the center of a 20 km (FGM) or 60 km (CGM) grid box, the elevation of eight additional points that were within the grid box were read off the maps—so that the model grid point was the center point of a 3×3 array of equally spaced points in the grid box. For each grid box, the nine points were used to create an average elevation and a standard deviation of elevations within that grid box. The average plus the standard deviation for each grid point produces a terrain height field referred to as a partial envelope orography (Wallace et al. 1983). For a full envelope, the standard deviation would be multiplied by 2.0 (referred to as the envelope parameter). An envelope orography is desirable because it is better able to produce the blocking effect of mountainous terrain, which is underestimated by a simple average over the grid box.

b. Smoothing and modification to ensure CGM/FGM compatibility

While the use of the envelope technique accomplishes some smoothing of the terrain fields, it is necessary to carry out some additional filtering to remove strong harmonics at $2\Delta x$ wavelengths. This was accomplished by applying a two-dimensional Shapiro (1970) filter on the terrain field. In order to avoid the need for a modified filter near the boundaries, the envelope terrain field was initially created

with an extra row of grid points on all sides of the desired final domain size. After the filter had been applied, these extra points were removed from the array to yield the smoothed, partial envelope CGM and FGM domains at the size required for the model.

The last step in the processing involved a modification to the FGM grid point elevations near the FGM/CGM interface. Zhang et al. (1986) have pointed out the strong need for consistency in the CGM/FGM overlap region (see Fig. 2) to help reduce noise generation, especially since the two-way interactive boundary condition results in an overspecification of the variables here. In the two-way interactive scheme, the FGM solution is used at CGM boundary points after the application of a nine-point average of the FGM variable centered on the CGM grid point. In order for these averaged FGM quantities to be consistent with the appropriate CGM quantity, the average FGM elevation using the same averaging operator must equal the CGM elevation at the coincident point. Zhang et al. (1986) describe a method for modifying the terrain field so that this condition is satisfied, and their method was employed on the terrain field used here. The resulting terrain fields after all this processing are those shown in Figs. 15 and 18.

References

- Anthes, R.A., 1978: The height of the planetary boundary layer and the production of circulation in a sea-breeze model. *J. Atmos. Sci.*, **35**, 1231-1239.
- Anthes, R.A., and T.T. Warner, 1978: Development of hydrodynamic models suitable for air pollution and other mesometeorological studies. *Mon. Wea. Rev.*, **106**, 1045-1078.
- Anthes, R.A., D. Keyser, and J.W. Deardorff, 1982: Further considerations on modeling the sea breeze with a mixed layer model. *Mon. Wea. Rev.*, **110**, 757-765.
- Arya, S.P.S., 1975: Geostrophic drag and heat transfer relations for the atmospheric boundary layer. *Quart. J. Roy. Meteor. Soc.*, **101**, 147-161.
- Bhumralker, C.M., 1975: Numerical experiments on the computation of ground surface temperature in an atmospheric general circulation model. *J. Appl. Meteor.*, **14**, 1246-1258.
- Benjamin, S.G., and T.N. Carlson, 1986: Some effects of surface heating and topography on the regional severe storm environment. Part I: Three-dimensional simulations. *Mon. Wea. Rev.*, **114**, 307-329.
- Colby, F.P., Jr., 1980: The role of convective instability in an Oklahoma squall line. *J. Atmos. Sci.*, **37**, 2113-2119.
- Colby, F.P., Jr., 1984: Convective inhibition as a predictor of convection during AVE-SEASAME II. *Mon. Wea. Rev.*, **112**, 2239-2252.
- Colby, F.P., Jr., and K.L. Seitter 1990: Super-Micro Computer Weather Prediction Model. Scientific Report No. 2. AFGL-TR-90-0174, 71 pp. ADA 230063
- Davies, H.C., 1976: A lateral boundary condition for multi-level prediction models. *Quart. J. Roy. Meteor. Soc.*, **102**, 405-418.
- Deardorff, J.W., 1977: A parameterization of ground surface moisture content for use in atmospheric prediction models. *J. Appl. Meteor.*, **16**, 1182-1185.
- Gauntlett, D.J., L.M. Leslie, and L.W. Logan, 1984: Numerical experiments in mesoscale prediction over southeast Australia. *Mon. Wea. Rev.*, **111**, 1170-1182.
- Haltiner, G.J., and R.T. Williams, 1980: *Numerical Weather Prediction and Dynamic Meteorology*. J. Wiley & Sons, 477 pp.
- Jackson, R.D., 1973: Diurnal changes in soil water content during drying. *Field Soil Water Regime*, Soil Sci. Soc. Amer., 37-55.

- Kalnay, E., W.E. Baker, M. Kanamitsu, and R. Petersen, 1991: Overview of the NMC analysis and modeling plans. Preprints, 9th Conference on Numerical Weather Prediction. Oct. 14-18, 1991, Denver, CO. Amer. Meteor. Soc., 5-10.
- Katayama, A., 1972: A simplified scheme for computing radiative transfer in the troposphere. *Tech. Rep. No. 6*, Dept. of Meteor., UCLA. 77 pp.
- Keyser, D., and R.A. Anthes, 1977: The applicability of a mixed layer model of the planetary boundary layer to real-data forecasting. *Mon. Wea. Rev.*, **105**, 1351-1371.
- Keyser, D., and L.W. Uccellini, 1987: Regional models: Emerging research tools for synoptic meteorologists. *Bull. Amer. Meteor. Soc.*, **68**, 306-320.
- Kurihara, Y. and M.A. Bender, 1980: Use of a movable nested-mesh model for tracking a small vortex. *Mon. Wea. Rev.*, **99**, 1792-1809.
- Lavoie, R.L., 1972: A mesoscale numerical model of lake-effect storms. *J. Atmos. Sci.*, **29**, 1025-1040.
- Lettau, H., and Davidson, 1957: *Explaining the Atmosphere's First Mile*, Pergamon Press, New York, Vol. I, II.
- McPherson, R.D., 1991: 2001—An NMC odyssey. Preprints, 9th Conference on Numerical Weather Prediction. Oct. 14-18, 1991, Denver, CO. Amer. Meteor. Soc., 1-4.
- Mellor, G.L. and A.F. Blumberg, 1985: Modeling vertical and horizontal diffusivities with the sigma coordinate system. *Mon. Wea. Rev.*, **113**, 1379-1383.
- Mesinger, F., Z.I. Janjić, S. Ničković, D. Gavrilov, and D.G. Deaven, 1988: The step-mountain coordinate: model description and performance for cases of Alpine lee cyclogenesis and for a case of Appalachian redevelopment. *Mon. Wea. Rev.*, **116**, 1493-1518.
- Mesinger, F., T.L. Black, D.W. Plummer, and J.H. Ward: Eta model precipitation forecasts for a period including tropical storm Allison. *Weather Fore.*, **5**, 483-493.
- Muench, H.S., 1983: Experiments in objective aviation weather forecasting using upper-level steering. *AFGL-TR-83-0328*, 44pp. ADA143393.
- Muench, H.S., 1988: Compositing local area forecast techniques. *AFGL-TR-88-0216*, 33 pp. ADA210802.
- Muench, H.S., and D.A. Chisholm, 1985: Aviation weather forecasts based on advection: Experiments using modified initial conditions and improved analyses. *AFGL-TR-85-0011*, 57 pp. ADA160369.
- Nickerson, E.C., 1979: On the simulation of airflow and clouds over mountainous terrain. *Bett. Atmos. Phys.*, **52**, 161-177.

- Nickerson, E.C., E. Richard, R. Rosset, and D.R. Smith, 1986: The numerical simulation of clouds, rain, and airflow over the Vosges and Black Forest mountains: A meso- β model with parameterized microphysics. *Mon. Wea. Rev.*, **114**, 398-414.
- Ookouchi, Y., M. Segal, R.C. Kessler, and R.A. Pielke, 1984: Evaluation of soil moisture effects on the generation and modification of mesoscale circulations. *Mon. Wea. Rev.*, **112**, 2281-2292.
- Pielke, R.A., 1984: *Mesoscale Meteorological Modeling*, Academic Press, 612 pp.
- Perkey D. J., and C.W. Kreitzberg, 1976: A time-dependent lateral boundary scheme for limited-area primitive equation models. *Mon. Wea. Rev.*, **104**, 744-755.
- Petersen, R.A., and J.D. Stackpole, 1989: Overview of the NMC production suite. *Wea. Forecasting*, **4**, 313-322.
- Schlesinger, R.E., L.W. Uccellini, and D.R. Johnson, 1983: The effects of the Asselin time filter on numerical solutions to the linear shallow water wave equations. *Mon. Wea. Rev.*, **111**, 455-467.
- Seitter, K.L., 1987: The specification of lateral boundary conditions in three-dimensional mesoscale numerical models. Final Report. AFGL-TR-87-0015, 129 pp. ADA179185.
- Seitter, K.L., and F.P. Colby, Jr., 1989: Super-Micro Computer Weather Prediction Model. Scientific Report No. 1. AFGL-TR-89-0239, 37 pp. ADA 216329
- Shapiro, R., 1970: Smoothing, filtering and boundary effects. *Rev. Geophys. Space Phys.*, **8**, 359-387.
- Sutton, O.G., 1953: *Micrometeorology*. McGraw-Hill Co., 333 pp.
- Wallace, J.M., S. Tibaldi and A.J. Simmons, 1983: Reduction of systematic forecast errors in the ECMWF model through the introduction of an envelope orography. *Quart. J. Roy. Meteor. Soc.*, **109**, 683-717.
- Warner, T.T., and N.L. Seaman, 1990: A real-time, mesoscale numerical weather-prediction system used for research, teaching, and public service at the Pennsylvania State University. *Bull. Amer. Meteor. Soc.*, **71**, 792-805.
- Wetzel, P.J., 1978: A detailed parameterization of the atmospheric boundary layer. *Atmos. Sci. Paper* 302, Colorado State University.
- Yamada, T., 1979: Prediction of the nocturnal surface inversion height. *J. Appl. Meteor.*, **18**, 526-531.
- Zeman, O., and H. Tennekes, 1977: Parameterization of the turbulent energy budget at the top of the daytime atmospheric boundary layer. *J. Atmos. Sci.*, **34**, 111-123.

Zhang, D.-L., and J.M. Fritsch, 1986: Numerical simulation of the Meso- β scale structure and evolution of the 1977 Johnstown flood. Part I. Model description and verification. *J. Atmos. Sci.*, **43**, 1913-1943.

Zhang, D.-L., H.-R. Chang, N.L. Seaman, T.T. Warner, and J.M. Fritsch, 1986: A two-way interactive nesting procedure with variable terrain resolution. *Mon Wea. Rev.*, **114**, 1330-1339.